Materials & Design 265 (2026) 115997

Contents lists available at ScienceDirect

Materials & Design

journal homepage: www.elsevier.com/locate/matdes

Tailoring high strength and heat resistance of Al-Ni-Fe-Zr near-eutectic alloy fabricated by laser powder bed fusion

Feng Li [a], Wei Zhang [a,*], Jiajia Shen [c,d], J.P. Oliveira [c,d], Dan Li [e], Chao Chen [e], Shaochuan Feng [f], Norbert Schell [g], Bart J. Kooi [b], Yutao Pei [a,*]

[a] *Advanced Production Engineering, Engineering and Technology Institute Groningen, Faculty of Science and Engineering, University of Groningen, Nijenborgh 3, 9747 AG, the Netherlands*
[b] *Nanostructured Materials and Interfaces, Zernike Institute for Advanced Materials, Faculty of Science and Engineering, University of Groningen, Nijenborgh 3, 9747 AG, the Netherlands*
[c] *UNIDEMI, Department of Mechanical and Industrial Engineering, NOVA School of Science and Technology, Universidade NOVA de Lisboa, 2829-516, Caparica, Portugal*
[d] *CENIMAT/I3N, Department of Materials Science, NOVA School of Science and Technology, Universidade NOVA de Lisboa, 2829-516, Caparica, Portugal*
[e] *State Key Laboratory of Powder Metallurgy, Central South University, Changsha 410083, China*
[f] *School of Mechanical Engineering, University of Science and Technology Beijing, Beijing 100083, China*
[g] *Helmholtz-Zentrum Hereon, Institute of Materials Physics, Max-Planck-Str. 1, Geesthacht 21502, Germany*

ARTICLE INFO

Keywords:
Laser powder bed fusion
Eutectic microstructure
Heat resistance
Mechanical properties
Synchrotron X-ray diffraction
Dislocation density

ABSTRACT

Aluminum alloys are widely used in lightweight applications but frequently suffer mechanical degradation at high temperatures due to phase coarsening. This study presents a novel Al-6.5Ni-1.4Fe-0.9Zr (wt.%) near-eutectic alloy, designed using thermodynamic principles and non-equilibrium solidification modeling to optimize both printability and mechanical performance. Fabricated via laser powder bed fusion, the alloy exhibits fine grains in both the horizontal and vertical planes, refined by Zr-induced nucleation, thereby minimizing microstructural anisotropy. The as-built alloy achieves a yield strength of 395 MPa and ultimate tensile strength of 560 MPa, primarily attributed to its refined ~300 nm cellular microstructure and high dislocation density. After 100 h of thermal exposure at 350 °C, the alloy maintains stable hardness and demonstrates superior heat resistance. *In situ* synchrotron X-ray diffraction was used to analyze dislocation density evolution using the Williamson-Hall method, revealing increased dislocation accumulation during tensile loading and partial recovery after aging. Nanosized $L1_2$-Al_3Zr precipitates with coherent interfaces contribute to thermal stability, exhibiting a low coarsening rate of 6.1 nm^3/s at 400 °C. These findings underscore the potential of the Al-6.5Ni-1.4Fe-0.9Zr alloy for high-performance applications in environments where long-term thermal stability and mechanical integrity are crucial.

1. Introduction

Aluminum (Al) alloys, owing to their high specific strength, are widely used as lightweight structural material in the sector of aircraft, automobile, automation and consumer electronics to reduce weight and save cost without sacrificing properties and service cycle, possessing more competitiveness than titanium alloys, copper alloys, and steels at ambient temperature [1,2]. Conversely, the superiority will vanish at elevated temperature, particularly over 200 °C, attributing to thermally induced precipitate coarsening and resultant softening, eventually leading to strength collapse [3–5]. Given the critical role that Al alloys play, applicable strengthening principles call for implementation.

Research on powder-based additive manufacturing (AM) of Al alloys is rapidly increasing due to its ability to produce complex component shapes, reduce weight, liberate design limitation, and enhance mechanical properties. Regarding the laser powder bed fusion (LPBF), ~822 publications were found in LPBF produced Al alloys from 2009 to 2019 investigated by Kusoglu et al. [6]. About 65% publications were

---

* Corresponding authors.
E-mail addresses: feng.li@rug.nl (F. Li), wei.zhang@rug.nl (W. Zhang), y.pei@rug.nl (Y. Pei).

https://doi.org/10.1016/j.matdes.2026.115997
Received 26 December 2025; Received in revised form 18 March 2026; Accepted 10 April 2026

near-eutectic Al-Si-(Mg) compositions, which results from minimizing solidification range and thereby reducing hot tearing susceptibility [7,8]. Eutectic reaction was shown to be a practical strategy to enhance the LPBF processability. Considering the 2000 series (Al-Cu) alloys that suffer cracking by LPBF, Pauly et al. increased the Cu content to Al-33Cu (wt.%) and achieved crack-free eutectic microstructure [9]. However, the prevalent Al-Si-(Mg) and Al-Cu alloys via LPBF are challenged by high temperature. Uzan et al. explored that the yield strength (YS) and ultimate tensile strength (UTS) of LPBF produced AlSi10Mg sharply declined from 204 and 358 MPa to 70 and 73 MPa, respectively at 300 °C, although the elongation (El) increased from 7.2 to 41.4% [10]. To enhance the high temperature performance of LPBF fabricated Al alloys, ceramic particles (TiB_2 [11], TiCN [12], and TiC [13]) act as heterogeneous nucleation sites, resulting in grain refinement and enhanced mechanical properties, noting deficiencies from the brittle byproducts (like Al_4C_3 [14]) and damage to plastic-toughness. Recently, Al-TM (transition metal) with near-eutectic composition were supposed to show promising heat resistance due to high volume fraction of thermally stable phases, particularly Al_3Ni [15] and $Al_{11}Ce_3$ [16], which provides sufficient strengthening phases and simultaneously ensures the LPBF processability. Deng et al. [15] obtained spherical nano-Al_3Ni in LPBF produced Al-5.7Ni eutectic alloy, maintaining a YS of 137 MPa at 300 °C, nearly twice as much as AlSi10Mg [10]. Furthermore, it was found that a nano thin layer of α-Al was sandwiched between each Al_3Ni fiber and the surrounding Al matrix [17]. This Al shell illustrated the coherent orientation with the Al_3Ni fiber, accordingly restricting the growth of the Al_3Ni phase. However, there is still room for strength enhancement of Al-Al_3Ni alloys when not only relying on eutectic Al_3Ni phases. Fe has been proven to be effective via solid solution strengthening, despite its low equilibrium solubility (0.025 at.%) [18]. For example, Mukai et al. produced Al-1.7Fe (at.%) alloy with supersaturated solid solution by non-equilibrium processing, achieving a high YS of 950 MPa [19]. Additionally, Al-1.75Fe-1.25Ni (wt.%) eutectic alloy by LPBF demonstrated excellent longstanding heat resistance under 300 °C because of the stable rod-like Al_9FeNi phases [20]. Nevertheless, large volume fraction of eutectic phases cannot withstand persistent thermal exposure at 400 °C or even higher temperature.

According to the literature, interfacial solute segregation has been demonstrated to be an effective method that couples the slow-diffusing solutes at the precipitates/matrix interfaces to inhibit the growth of strengthening phases. It was shown that Sc/Zr segregated at the interfaces with coherent orientations can stabilize the nanoprecipitates by reducing the interfacial energy and blocking the *trans*-interface diffusion, thereby resulting in enhanced mechanical properties and high creep resistance [21,22]. In particular, the synergistic effects of $L1_2$-$Al_3(Sc, Zr)$ strengthened α-Al phase and coarsening-resistant Al-$Al_{11}Ce_3$ eutectic, due to interfacial Sc and Zr segregation, lead to excellent 1000 h creep resistance at 400 °C in the as-cast Al-1.5Ce-0.14Sc-0.03Zr (at.%) alloy [21]. While Sc is a more potent strengthener than Zr attributing to the faster precipitation kinetics of Sc, Zr is more economically practical and has stronger interfacial segregation behavior, contributing to enhanced heat resistance [23,24]. Pandey et al. provided clear evidence of Zr segregation at the eutectic Al_3Ni and Al matrix interface via atom probe tomographic technique, which improved the mechanical properties and reduced the coarsening rate [25].

After a thorough analysis, we have designed a novel additively manufactured Al-6.5Ni-1.4Fe-0.9Zr (wt.%) alloy that integrates a large-volume fraction of heat-resistant eutectic Al_3Ni phases and nano-sized $L1_2$-Al_3Zr strengthening precipitates, making it highly promising for high-temperature applications. The sub-micron cellular eutectic phases not only ensure the processability of LPBF but also contribute significantly to the mechanical properties through precipitation strengthening, with Fe providing additional reinforcement. Meanwhile, the nano $L1_2$-Al_3Zr precipitates enhance resistance to high-temperature coarsening, owing to the synergistic effect with the coherently strengthened α-Al phase. We investigate the microstructural characteristics, mechanical properties, and thermal stability of the LPBF-produced Al-6.5Ni-1.4Fe-0.9Zr alloy, with the Scheil-Gulliver solidification model [26] aiding in the design process. Furthermore, the evolution of dislocation density in the Al matrix during *in situ* loading, both in the as-printed and heat-treated states, is evaluated using high-energy synchrotron X-ray diffraction (SXRD). By revealing how cellular eutectic microstructure and coherent nanoprecipitates synergistically govern strength and thermal stability, this work advances cost-effective heat-resistant aluminum alloy development.

Table 1
Chemical composition of the Al-Ni-Fe-Zr powder.

Elements	Ni	Fe	Zr	O	Al
Wt.%	6.45	1.37	0.85	0.05	Balance

2. Materials and experiments

2.1. Materials fabrication

The pre-alloyed powder was prepared using the gas-atomized technique from a mixture of pure Al, Al-10Ni, Al-10Fe, and Al-10Zr master alloys. The stoichiometric composition of the Al-Ni-Fe-Zr powder was obtained via the inductively coupled plasma-atomic emission spectrometry (ICP-AES) and listed in Table 1, abbreviated as Al-6.5Ni-1.4Fe-0.9Zr. Fig. 1(a) shows the spherical powder shape with a Hall flow rate of 55.25 s/50 g (ISO 4490). Additionally, the particle size distribution, with Dv(10) = 23.1 μm, Dv(50) = 39.4 μm, and Dv(90) = 62.8 μm, is presented in Fig. 1(b). The cross sections of the powders exhibit a mixture of cellular (Fig. 1(c and d)) and lamellar (Fig. 1(e and f)) structures. Sample printing was performed with an SLM®125 HL printer (SLM Solutions, Germany) with a 400 W IPG Yb fiber laser under high purity argon atmosphere. An Al alloy plate (125 × 125 × 25 mm) was used as a building substrate with a preheating temperature of 200 °C. A process window was explored with laser power ranging from 200 to 380 W and scanning speed from 600 to 2600 mm/s, while the layer thickness and hatch spacing were fixed at 30 μm and 100 μm, respectively. As shown in Fig. S1 of the Supplementary Materials, the highest relative density reached 99.5% and the maximum Vickers hardness reached ~177.1 HV at 380 W and 1800 mm/s. The specimens printed with this parameter set were used for subsequent microstructural characterization and mechanical testing. Fine cellular structures were consistently observed across the different LPBF parameter sets investigated, see Fig. S2. A 67° layer rotation and stripe scanning strategy were adopted to achieve high density fabrication. After printing, the specimens were removed from the building substrate by wire electrical discharge machining (WEDM).

2.2. Microstructure characterization

Optical microscopy (OM) images were collected on an Olympus VANOX-T AH-2. The sample microstructures were observed using a scanning electron microscope (SEM, Tescan LYRA, Czech Republic) with a backscattered electron (BSE) detector and an electron backscatter diffraction (EBSD) system. Samples for OM and SEM were initially prepared by mechanical grinding with SiC abrasive paper to achieve a flat surface, followed by polishing to a 1 μm finish using colloidal silica. OM samples were subsequently etched for 3 to 5 s using Keller's reagent (a solution of 2.5 ml HNO_3, 1.5 ml HCl, 1 ml HF, and 95 ml distilled water). For SEM and EBSD analysis, electropolishing was performed using a mixture of perchloric acid and ethanol in a 9:1 vol ratio at 15 V and −30 °C for 10 to 20 s. Transmission electron microscopy (TEM, JEOL JEM-2200FS, Japan) was performed to analyze the precipitate morphology and crystallography information. Nanoscale

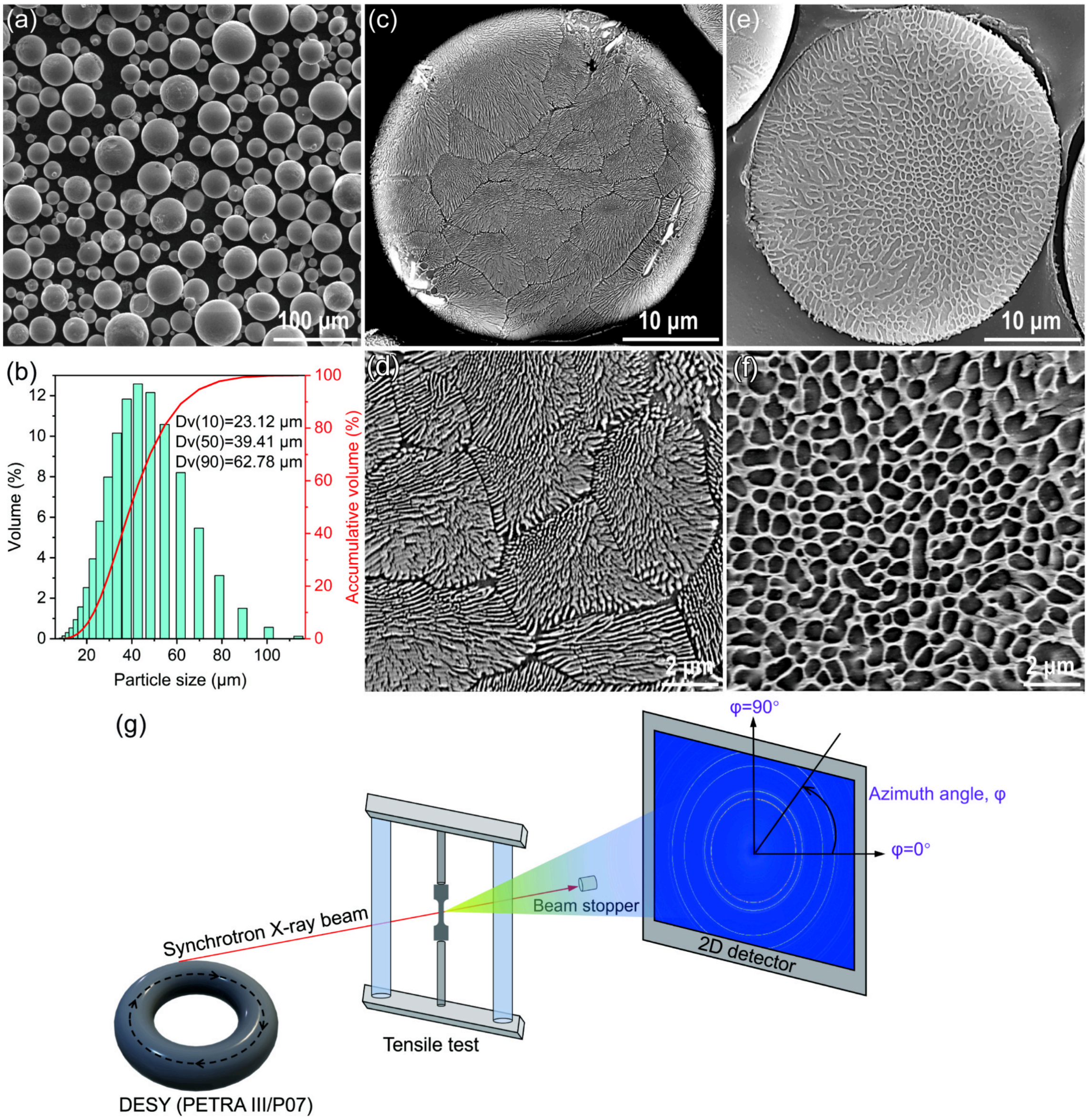

Fig. 1. (a) SEM image showing the powder morphology, (b) powder particle size distribution, BSE images showing (c, d) lamellar and (e, f) cellarer eutectic microstructure of powders, and (g) schematic set-up of *in situ* SXRD experiment.

microstructural characterization was conducted using an FEI Talos F200X S/TEM operated at 200 kV, coupled with energy dispersive x-ray spectroscopy (EDS) for local chemical composition analysis. In addition, the NanoMEGAS ASTAR system integrated with the TEM was used to enable automated crystal orientation and phase mapping at the nanoscale. TEM specimens were prepared by focused ion beam (FIB) slicing (FEI Helios G4 CX dual-beam microscope, USA).

2.3. Heat treatment and mechanical testing

Rectangular samples of LPBF fabricated Al-6.5Ni-1.4Fe-0.9Zr alloy were cut in the dimension of 6 × 6 × 3 mm and subsequently aging-treated at 250, 300, 350, and 400 °C for 0–100 h holding time. Following ASTM E384-08a, microhardness tests were performed at 300 g load for 10 s. Fifteen measurements were taken for each sample. To investigate the mechanical performance of both the as-fabricated specimens and those aged for 6 h at 300 and 400 °C, dog-bone tensile samples were prepared with their long axes parallel to the laser scanning direction. These samples were cut to gauge dimensions of 11.5 × 3.5 × 1 mm using WEDM, after which the top, bottom, and lateral grip surfaces were ground with SiC abrasive papers up to 4000 grit. All tensile tests were conducted at room temperature (RT) using an MTS Alliance machine at a strain rate of 1×10^{-3} s^{-1}, with a video extensometer. Additionally, high-temperature tensile experiments were conducted at 200, 300, and 350 °C on an Instron 5989 machine equipped with a 50 kN load cell at a strain rate of 1×10^{-3} s^{-1}. Strain gauges measured deformation at 200 and 300 °C, while strain at 350 °C was calculated from crosshead displacement as the strain gauges could not function at this temperature.

2.4. In situ SXRD experiment

SXRD experiments were performed at the P07B High Energy Beamline of PETRA III/DESY for phase identification and dislocation density calculation. To reveal the bulk microstructural information in transmission mode, a high-energy beam with a photon energy of 87.10 keV

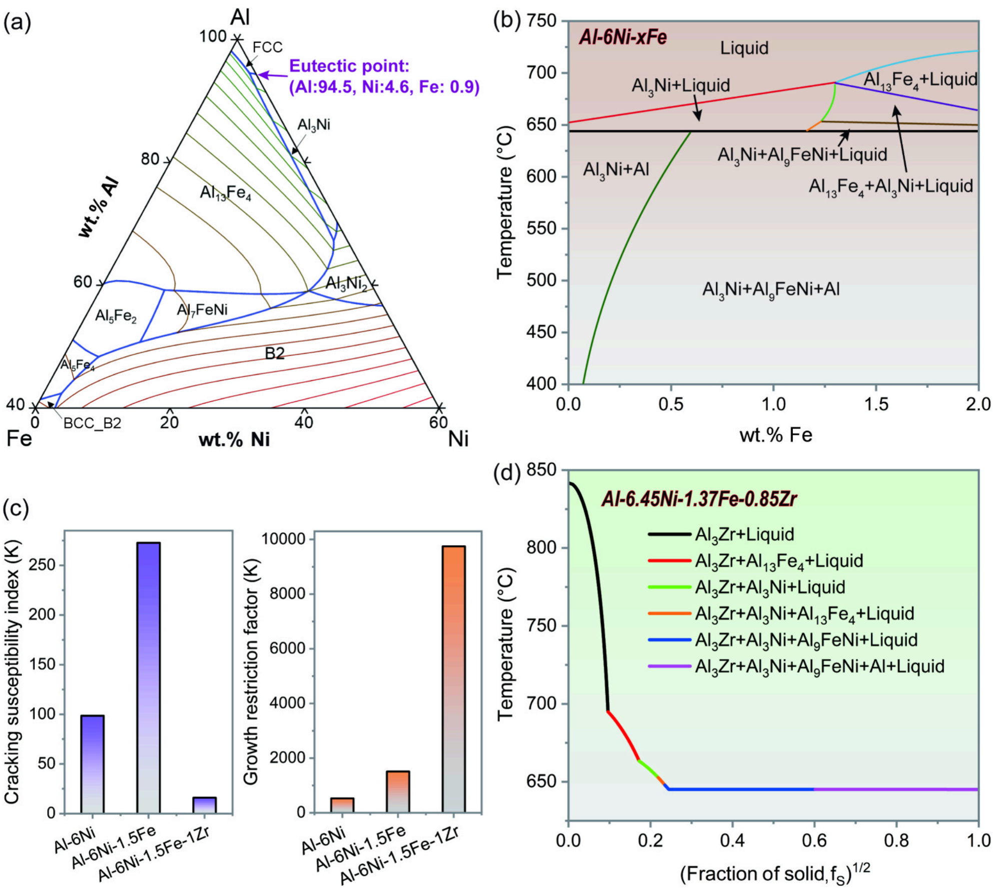

Fig. 2. Design strategies of Al-Ni-Fe-Zr alloy: (a) The isothermal section diagram of ternary Al-Ni-Fe system, (b) Al-6Ni-xFe (x = 0–2 in wt.%) pseudo-binary phase diagram, (c) growth restriction factors and cracking susceptibility indexes of Al-6Ni, Al-6Ni-1.5Fe, Al-6Ni-1.5Fe-1Zr alloys, and (d) solidification range of Al-6.5Ni-1.4Fe-0.9Zr alloy based on the Scheil-Gulliver model. The phase diagrams (a, b) are generated by Pandat® software.

(equivalent to a wavelength of 0.14235 Å) was employed with a beam size of 700 × 700 μm^2. A 2D PerkinElmer fast detector with a pixel size of 200 × 200 μm^2 was utilized to acquire the Debye-Scherrer diffraction rings under various stress/strain levels. Before *in situ* experiments, LaB$_6$ standard was employed to calibrate instrumental peak broadening from the beamline optics, and determine the sample-to-detector distance (1226 mm). Fig. 1(g) provides an illustration of the SXRD experimental setup during *in situ* tensile testing. Following the acquisition of the 2D images, the raw data underwent post-processing through a hybrid approach involving Fit2D and Rietveld refinement using MAUD software.

3. Results

3.1. Alloy by design

To understand the solidification behavior of ternary Al-Ni-Fe alloy, Pandat® thermodynamic software was used to calculate the ternary Al-Ni-Fe eutectic point of 94.54Al-4.59Ni-0.87Fe (wt.%) as shown in Fig. 2 (a). The pseudo-binary phase diagram of Al-6Ni-xFe alloy reveals the change of phases with increasing Fe content (Fig. 2(b)). To avoid the formation of the coarse Al$_{13}$Fe$_4$ phase, the mass fraction of Fe should be lower than ~1.3 wt%. At the final stage of solidification, eutectic Al/Al$_3$Ni and thermally stable Al$_9$FeNi phases are supposed to be present. The printability of eutectic alloys was further analyzed. Hot cracking susceptibility is a practical measure of LPBF printability, since cracks often form during the terminal stage of solidification and limit build integrity. It is quantified using crack susceptibility index (CSI), defined as the absolute slope $\left|dT/d(f_S)^{1/2}\right|$ evaluated near $(f_S)^{1/2} = 1$, which can be expressed as [26]:

$$\left\{ \underset{(separation)}{\frac{d\varepsilon_{local}}{dt}} > \underset{(growth)}{\sqrt{1-\beta}\,\frac{d\sqrt{f_S}}{dT}\,\frac{dT}{dt}} + \frac{d}{d_z}\left[\left(1-\underset{(feeding)}{\sqrt{1-\beta}}\sqrt{f_S}\right)v_z\right]\right\}_{\sqrt{f_S}\to 1} \tag{1}$$

where ε_{local} is the local strain in the mushy zone, t is time, β is the solidification shrinkage, f_S is the solid fraction, T is temperature, z is the axial direction, and v_z is the liquid feeding velocity along grain boundary (GB). CSI is obtained by calculating the solidification path and then measuring the local steepness of the T versus $(f_S)^{1/2}$ curve close to complete solidification. The solidification path was calculated using Pandat® thermodynamic software based on the designed alloy composition. A smaller CSI indicates lower hot cracking susceptibility and therefore better printability. A higher growth restriction factor (Q) value leads to smaller grain size and enhances mechanical properties due to refined microstructure, which is calculated by the following equation [27,28]:

$$Q = \left(\frac{\partial(\Delta T_{CS})}{\partial f_S}\right)_{f_S \to 0} \tag{2}$$

where ΔT_{CS} stands for constitutional undercooling affecting grain nucleation and growth. The calculation results indicate that Fe solute

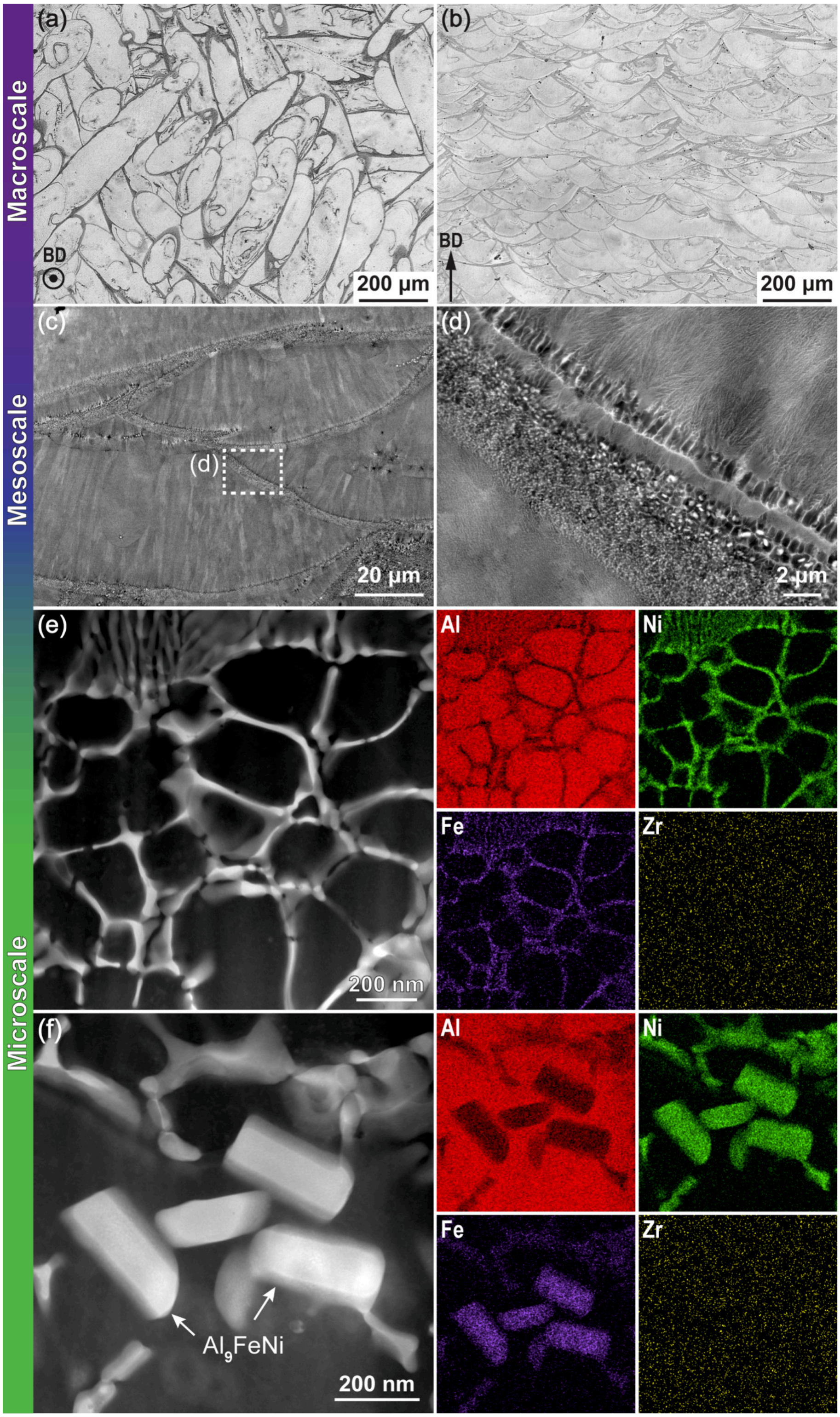

Fig. 3. Multiscale characterizations of as-printed Al-6.5Ni-1.4Fe-0.9Zr alloy. OM images (a) perpendicular to the BD and (b) paralleled to the BD. (c) SEM-BSE image and (d) corresponding enlarged image. STEM-HAADF micrographs and corresponding EDS maps (Al, Ni, Fe, and Zr) showing (e) cellular structure and (f) Al_9FeNi particles.

contributes minimally to grain refinement, whereas Zr significantly enhances it.

The cracking susceptibility indexes and growth restriction factors of Al-6Ni, Al-6Ni-1.5Fe, and Al-6Ni-1.5Fe-1Zr alloys were calculated and plotted in Fig. 2(c). Compared with Al-6Ni-1.5Fe, binary Al-6Ni eutectic alloy demonstrates lower cracking susceptibility. Adding Zr significantly decreases the CSI, proving the feasibility of crack-free printing. Additionally, the solute elements of Ni, Fe, and Zr have separate effects on the grain size in Al alloys. Evaluating the impact of solute additions on grain growth provides the fundamental prediction of the mechanical properties. As discussed above, the near-eutectic Al-6.5Ni-1.4Fe-0.9Zr alloy could have both good printability and competitive mechanical performance. The solidification behavior of the alloy is plotted in Fig. 2(d). The possible thermostatic eutectic reaction (Liquid → α-Al + Al_3Ni/Al_9FeNi) is found at the final stage of solidification, which substantially shrink the solidification range. Consequently, this reduction leads to a shorter duration of the mushy zone, thereby minimizing the thermal stresses that can cause solidification cracking.

3.2. Heterogeneous as-built microstructure

The multiscale characterizations in Fig. 3 demonstrate the crack-free printing and heterogeneous microstructure. Fig. 3(a and b) show the OM images of the as-fabricated samples viewed perpendicular and parallel to the building direction (BD), respectively. Both directions exhibit typical LPBF features solidified from semi-circular melting pool (MP) and scanning tracks are evident on the top plane that is perpendicular to the BD. The single-track diameter and hatching distance both are ~100 μm, in good agreement with the processing parameters. The SEM images in Fig. 3(c and d) illustrate the mesoscale structure features at the melting pool boundary (MPB) and in the melting pool interior (MPI). Fig. 3(c) displays a distinct MPB with cellular structures formed due to the rapid solidification typical of LPBF, which enhances strength by refining grain size and limiting dislocation motion [29]. Fig. 3(d) reveals fine Al_9FeNi precipitates at the MPB, which stabilize the microstructure at elevated temperatures by preventing grain coarsening. The STEM high-angle annular dark-field (HAADF) imaging combined with EDS mapping (Fig. 3(e and f)) provides a closer view of nanoscale chemical partitioning in the as-fabricated alloy. In Fig. 3(e), a submicron cellular morphology with an average diameter of ~300 nm is observed. In contrast to the fibrous morphology reported for cast Al-6Ni [30], the present alloy exhibits distinct cellular characteristics, where the cell interiors are Al-rich and the cell walls are enriched in Ni, consistent with an Al_3Ni-rich eutectic network. A weak but detectable Fe enrichment is also observed along parts of the cell walls, which suggests that a small fraction of Al_9FeNi is present within the wall network. Fig. 3(f) further reveals the Al_9FeNi phase more clearly as regular plate-like particles with strong Fe and Ni signals, which corresponds well to the particle-rich region at the MPB seen in Fig. 3(d). The Zr map remains relatively uniform at the present spatial resolution, suggesting that Zr is predominantly retained in the Al matrix rather than concentrated in the Ni- and Fe-rich intermetallic phases.

The EBSD analyses of the LPBF processed Al-6.5Ni-1.4Fe-0.9Zr alloy demonstrate notable differences in microstructural features between the cross sections perpendicular and parallel to the BD, see Fig. 4. The inverse pole figure (IPF) maps in Fig. 4(a and e) and the grain size distribution charts in Fig. 4(c and g) indicate that the grains oriented perpendicular to the BD are finer and more equiaxed, with an average size of 3.4 μm, compared to the slightly larger average grain size of 4.3 μm along the BD. This refined grain structure can be attributed to the rapid cooling rates and the effective grain refinement action of Zr during solidification. Zr enhances grain nucleation by forming fine dispersoids that inhibit grain growth, resulting in a more uniform and refined microstructure. The Kernel average misorientation (KAM) maps in Fig. 4(b and f) provide additional insights into the local misorientation distribution, which is generally proportional to an increased geometrically necessary dislocation (GND) density. The blue regions in the KAM maps, primarily at the MPB or where MPs overlap, indicate low local misorientation and thus a relatively low GND density, while the green areas, found in the MPI, show higher misorientation and a higher GND density.

MPBs and overlap regions experience stronger thermal cycling, which can promote recovery in the Al matrix. As a result, stored deformation and local misorientation are reduced. MPIs undergo less thermal resetting, so strain gradients are more readily retained, giving higher KAM values and a correspondingly higher GND density. This difference is more pronounced on the cross section perpendicular to the BD, due to the directional solidification pattern and higher cooling rates, which lead to a more heterogeneous dislocation distribution. As seen in Fig. 4(d and h), PF images further reveal differences in crystallographic texture between the two directions. The stronger texture observed perpendicular to the BD suggests a preferential grain orientation due to the layer-by-layer nature of the LPBF process, which aligns grains along the thermal gradients. Moreover, the finer grain structure achieved through Zr addition reduces the degree of microstructural anisotropy and improves mechanical isotropy. As shown in Fig. S3, tensile loading parallel to the BD gives slightly higher strength, whereas loading perpendicular to the BD results in better ductility. The strength advantage along the BD is attributed to texture-controlled slip resistance, while the equiaxed grain morphology in the perpendicular direction promotes more uniform strain accommodation and delays strain localization, hence improving ductility.

The as-printed alloy exhibits a submicron cellular microstructure as seen in Fig. 5(a). The NanoMEGAS ASTAR technique provides TEM-based orientation and phase mapping, serving as a TEM-EBSD analogue, and reveals that adjacent cells present distinct crystallographic orientations rather than a single continuous orientation field (Fig. 5(b)). The GB map in Fig. 5(c) shows that high-angle boundaries delineate the cell walls and outline individual cells, whereas low-angle boundaries are concentrated within the cell wall regions, giving the cellular network a GB-like character that can hinder slip transfer and contribute to Hall-Petch-type strengthening. The phase map in Fig. 5(d) further presents an Al-rich cell interior and Al_3Ni concentrated along the walls, so deformation is constrained not only by misorientation boundaries but also by Al/Al_3Ni phase interfaces distributed along the cellular walls. A HRTEM image of the Al matrix is shown in Fig. 5(e), with an accompanying SAED pattern that confirms the crystalline nature of the matrix along the [011] zone axis. Fig. 5(f) presents the corresponding IFFT of the HRTEM image, revealing the distribution of dislocations induced during the rapid solidification process.

3.3. Artificial aging

The Vickers microhardness of LPDF printed Al-6.5Ni-1.4Fe-0.9Zr alloy samples was measured as a function of aging time from 0 to 100 h at aging temperature ranged from 250 to 400 °C, as displayed in Fig. 6. At 250 °C, the hardness decreases least with aging time. The peak aging treatment at 300 °C for 1 h results in a microhardness of 181 ± 7 HV, compared to the as-built microhardness of 177 ± 11 HV. After peak aging, the hardness starts to decrease with longer isothermal exposure at 300 °C. A similar trend is found for 350 °C aging, where all the hardness values are lower than the as-printed one. The Al-6.5Ni-1.4Fe-0.9Zr alloy undergoes further over-aging at 400 °C, resulting in a steeper decline in hardness. After 100 h of aging, the microhardness decreases by ~11% at 250 °C and by ~18% at 350 °C. In contrast, by aging at 400 °C for 100 h, the Vickers microhardness decreases by ~32% to 121 ± 4 HV, which is comparable to LPBF Al-5.5Fe-0.8Mo-0.9Si-0.8Zr under the same condition (~32.4%) [31], as summarized in Table S1. After 100 h of aging at 350 °C, the hardness decrease is ~18%, which remains lower than the ~28.5% reported for LPBF Al-5.9Ni-0.3Sc after 50 h [32], and is comparable to the ~17% decrease reported for LPBF Al-1.8Fe-1.3Ni after 48 h [20], despite the longer exposure time in the present study. Therefore, the present alloy shows good hardness retention during long-term thermal exposure.

Thermal exposure at 400 °C for 100 h leads to significant microstructural coarsening in the LPBF Al-6.5Ni-1.4Fe-0.9Zr alloy compared to the as-printed state. As seen in Fig. 7(a), the overall cellular structure observed in the as-built alloy has evolved, and the precipitates have coarsened. The intermetallic phases, particularly Al_9FeNi, have grown substantially, as seen in Fig. 7(b), with larger and more widely spaced particles, contrasting with the finer, more uniformly distributed rod-like precipitates characteristic of the rapid solidification in the as-built alloy. Fig. 7(c) highlights the formation of nano-sized Al_3Zr particles, which

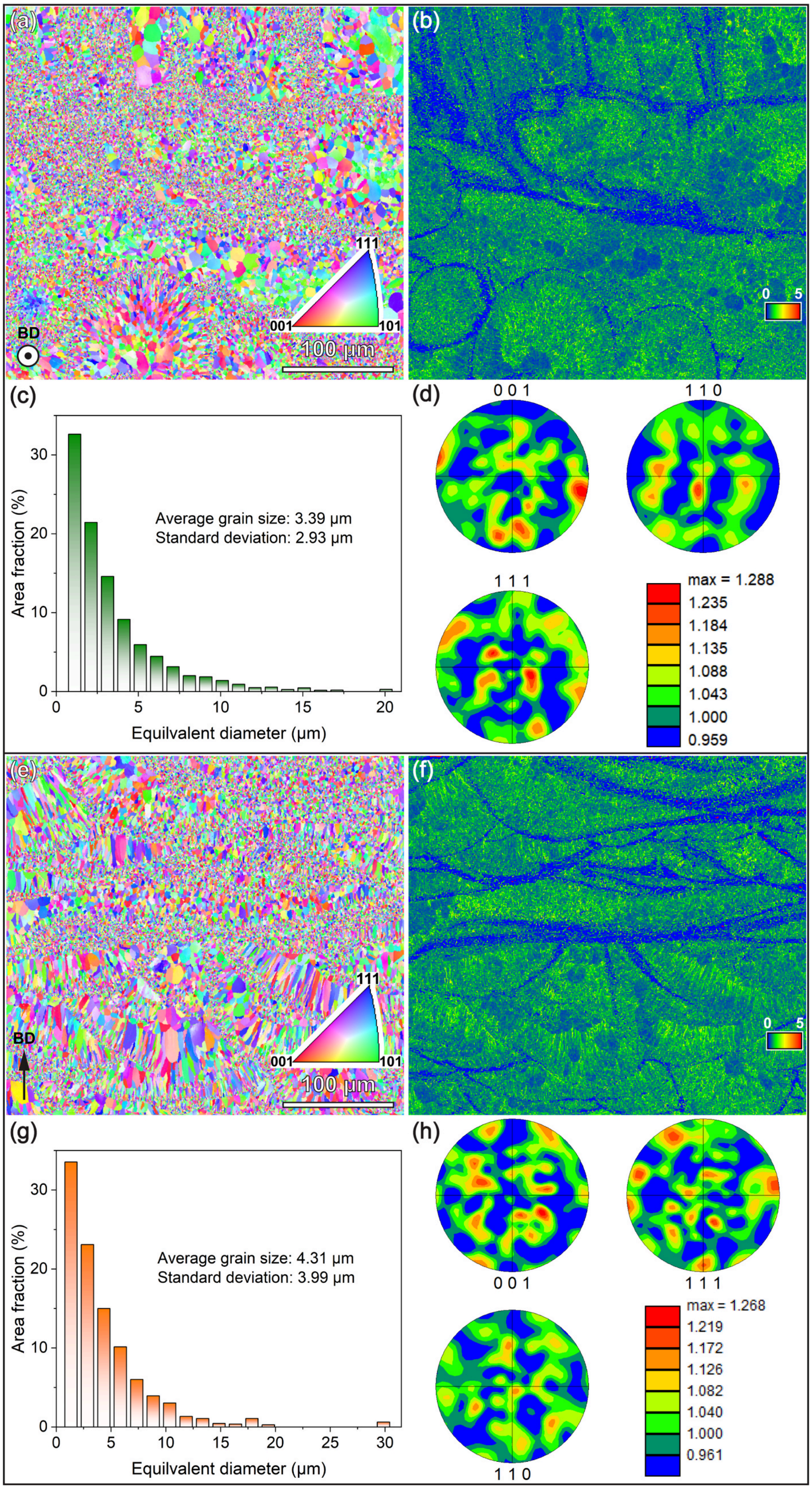

Fig. 4. EBSD results of the as-built specimens (a-d) normal to the BD and (e-h) along the BD. (a, e) IPF maps, (b, f) KAM maps, (c, g) grain size distribution charts, and (d, h) Pole figure (PF) images.

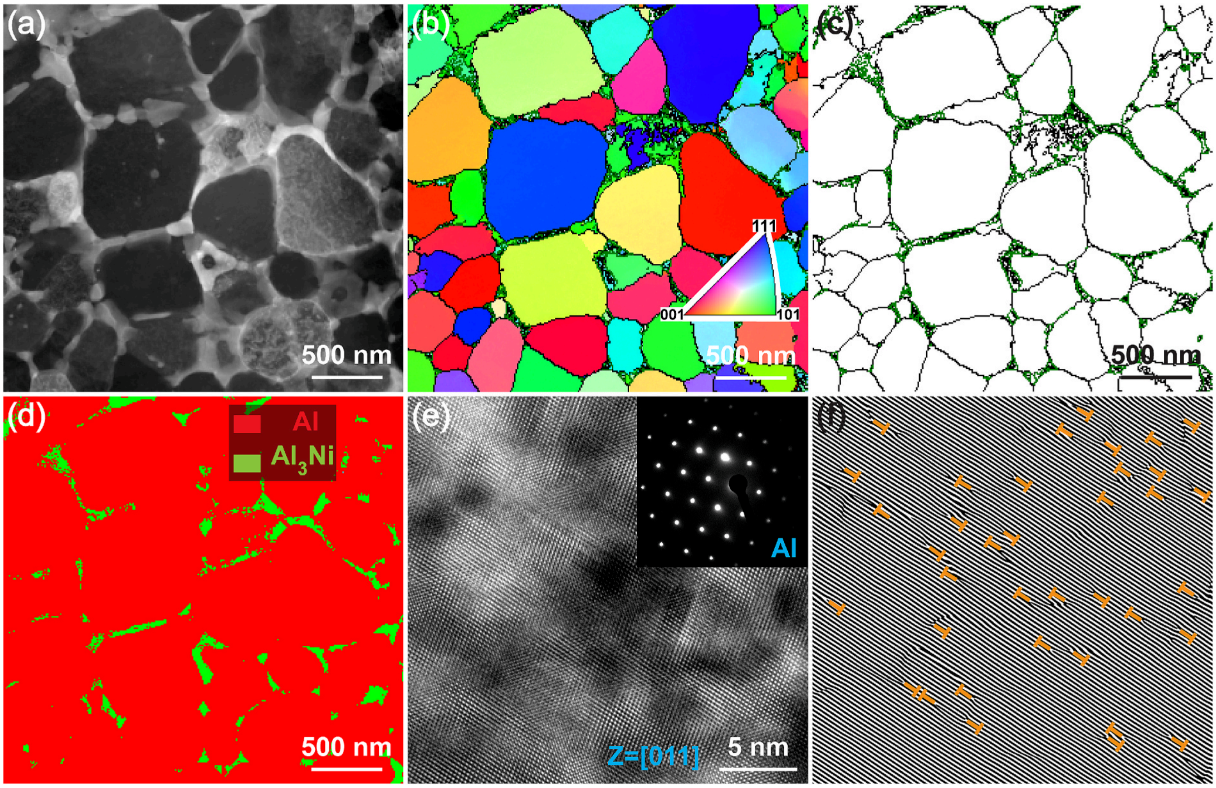

Fig. 5. (a) STEM-HAADF image of the submicron cells in the as-printed alloy. Precession electron diffraction in TEM was performed using the NanoMEGAS ASTAR system in the same region to obtain cellular-scale orientation, boundary and phase information: (b) orientation map with GB, highlighting orientation differences between adjacent cells; (c) GB map where green lines mark low-angle GBs of 2–15° and black lines mark high-angle GBs above 15°, indicating that cellular boundaries exhibit similar GB feature; (d) phase map with Al in the cell interior and Al_3Ni concentrated along the cell walls. (e) High-resolution TEM (HRTEM) image of the Al matrix, with the inset displaying the corresponding selected area electron diffraction (SAED) pattern. (f) The inverse fast Fourier transform (IFFT) of (e) showing dislocation distribution in the Al matrix. (For interpretation of the references to colour in this figure legend, the reader is referred to the web version of this article.)

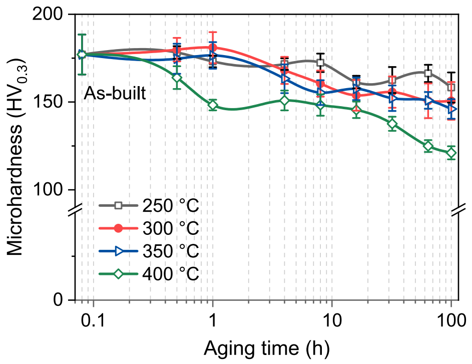

Fig. 6. Evolution of Vickers microhardness for the as-built Al-6.5Ni-1.4Fe-0.9Zr alloy during aging treatments from 0.5 to 100 h at 250–400 °C temperatures.

remain relatively stable at high temperatures and help to inhibit grain growth.

TEM analyses in Fig. 8 reveal the characteristic structures of Al_3Zr, Al_3Ni, and Al_9FeNi phases in the sample after 400 °C over-aging for 100 h. HRTEM image in Fig. 8(a) shows the nanoscale $L1_2$-Al_3Zr precipitates. The incident electron beam is parallel to the [0 0 1] zone axis of the Al matrix and $L1_2$-Al_3Zr. The corresponding FFT pattern in Fig. 8(b) presents the superlattice reflections of Al_3Zr phase and demonstrates that the precipitate is fully coherent with the matrix for $[0\,0\,1]_{Al}//[001]_{Al_3Zr}$. When imaged along $[\overline{11}\ 3]_{Al}$ zone axis, HRTEM micrograph in Fig. 8(c) and diffraction spots in Fig. 8(d) further provide evidence that the Al_3Zr precipitates are also coherent for $[\overline{11}\ 3]_{Al}//[\overline{11}3]_{Al_3Zr}$ and therefore there is a cube-on-cube orientation relationship between precipitate and matrix. To obtain the characteristic structure at Al/Al_3Ni, HRTEM images in Fig. 8(e and f) were taken from $[2\overline{1}1]_{Al_3Ni}$ zone axis showing inapparent orientation relationship with Al matrix. As observed in Fig. 8(g), electron diffraction patterns of orthorhombic Al_3Ni were indexed using the CrysTBox software [33]. Fig. 8(h) was taken at the Al/Al_9FeNi interface under the $[\overline{1}\ 31]_{Al}$ zone axis, which is parallel to the $[0\overline{1}0]_{Al_9FeNi}$ zone axis. The indexed diffraction spots of Al and Al_9FeNi phases are depicted in Fig. 8(i) and (j), respictively.

3.4. *In situ SXRD analysis*

SXRD is a powerful tool in material science for accurately identifying phases and quantitatively analyzing crystal structures, owing to its superior resolution and high-intensity X-ray source. Fig. 9 displays the SXRD patterns for the as-printed and heat-treated samples. Based on the peak positions, compositional elements, and intensities, as well as the PDF cards from the ICDD database (#03-065-2869, #00-002-0416, #04-014-7251 and #04-015-2439), four main phases have been identified as α-Al, Al_3Ni, Al_9FeNi and Al_3Zr.

Further analysis of mechanical responses demands the knowledge of dislocation density, which is calculated by classical Williamson-Hall method based on the full width at half maximum (FWHM) of the diffraction peaks. The peak broadening of diffraction reflection is mainly attributed to the average crystallite size (D) broadening and strain (ε) broadening [34–36]:

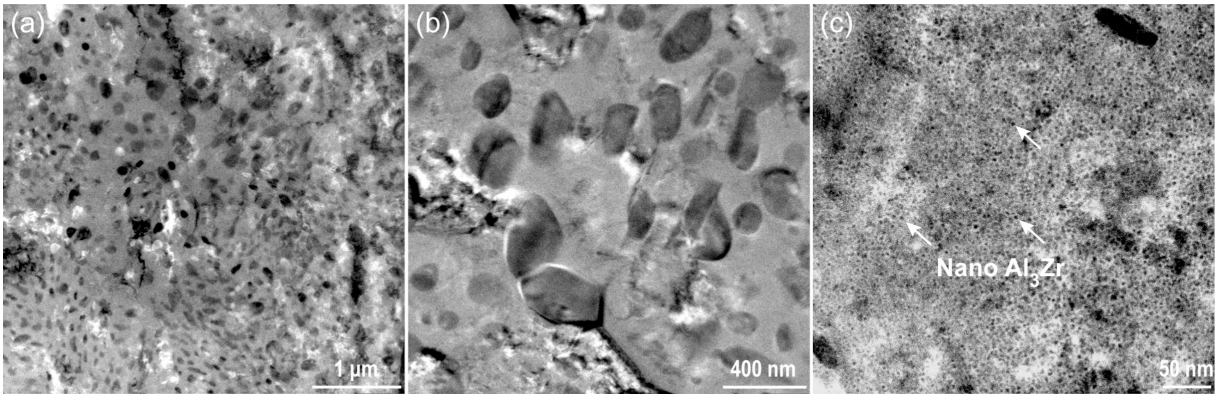

Fig. 7. BF-TEM micrographs of the LPBF Al-6.5Ni-1.4Fe-0.9Zr alloy after thermal exposure at 400 °C for 100 h: (a) Overview, (b) coarsened precipates, and (c) nano-sized Al_3Zr particles.

$$\beta cos\theta_{hkl} = 4\varepsilon sin\theta_{hkl} + \frac{K\lambda}{D} \tag{3}$$

where β denotes the FWHM of SXRD spectrum (radian), θ_{hkl} is the Bragg angle of the diffraction peak, K is a constant 0.9, and λ is the diffraction wavelength. The values of D and ε at every applied strain can be calculated by the intercept and slope from the linearly-fitted lines of $\beta cos\theta_{hkl}$ as a function of $4sin\theta_{hkl}$. In the Williamson-Hall analysis, the crystallite size represents the average length scale over which the crystal lattice remains coherently diffracting, a domain that can be subdivided by dislocation structures and subgrain boundaries within a single grain. It is therefore not equivalent to the EBSD grain size in Fig. 4, the latter being a geometric measure of orientation-defined grains delimited by high-angle boundaries. In addition, stacking fault broadening is not separated in basic Williamson-Hall treatment and, if present, is folded into the fitted crystallite size and microstrain terms as extra reflection dependent broadening. Given the high stacking fault energy of Al, its contribution should be minor in the present alloy. The dislocation density (ρ) can be determined by the following equation [36]:

$$\rho = 16.1\left(\frac{\varepsilon}{b}\right)^2 \tag{4}$$

Fig. 10 shows the evolution of dislocation density in the LPBF Al-6.5Ni-1.4Fe-0.9Zr alloy during *in situ* tensile deformation, comparing the as-built condition with heat-treated conditions at 300 °C and 400 °C. The FWHM curves in Fig. 10(a, d, and g) provide basic insights into microstructural changes, revealing broadening of diffraction peaks as strain increases, which indicates higher micro strain and defect density in the material. The FWHM values are plotted as a function of true strain for different crystallographic planes of Al matrix (indexed as (1 1 1), (2 0 0), (2 2 0), and (3 1 1)). These four reflections correspond to the strongest peaks of the α-Al matrix and were selected to ensure good counting statistics and minimal interference from minor intermetallic peaks in this Al-rich alloy. Their spread across a wide 2θ range provides sufficient data points to constrain the Williamson-Hall linear fit and separate crystallite size and microstrain broadening contributions. As true strain increases, the FWHM generally rises, particularly for the (2 2 0) and (3 1 1) planes, which indicates an increase in dislocation density due to the accumulation of plastic deformation. The linear fits in Fig. 10 (b, e and h), based on Williamson-Hall plots, allow for the separation of strain-induced broadening from crystallite size effects. The slope of the fit corresponds to strain, while the intercept reflects changes in crystallite size. Such approach helps quantify the evolution of dislocation density as a function of strain.

In the as-built condition (Fig. 10(c)), the dislocation density increases sharply up to around 3.5×10^{15} m^{-2} with increasing strain, especially after 2% true strain. The rapid rise in dislocation density indicates that the LPBF process induces a highly strained microstructure, which is typical due to the rapid solidification and cooling rates inherent in LPBF. When subjected to heat treatment at 300 °C for 6 h (Fig. 10(f)), the dislocation density still increases during loading, but the maximum density is significantly lower than that in the as-built state, suggesting partial recovery and dislocation annihilation. This behavior is likely due to the relaxation of internal stresses and recrystallization processes occurring during the heat treatment. At 400 °C for 6 h (Fig. 10(i)), the dislocation density increases at a slower rate during tensile straining and reaches a peak around 2.5×10^{15} m^{-2}, indicating further recovery and softening of the alloy. The reduced dislocation accumulation reflects a more thermodynamically stable microstructure, primarily due to the coarsening of precipitates and a reduction in the density of cellular structures. Such heat treatments at elevated temperatures typically alter phase stability and precipitate distribution, reducing dislocation density and improving ductility at the potential expense of strength [37,38]. These observations demonstrate the influence of post-processing on the mechanical performance of LPBF Al alloys, showcasing how heat treatments can be used to fine-tune the microstructure for optimized strength and ductility.

3.5. *Tensile properties*

The representative engineering strain–stress curves in AM Al-6.5Ni-1.4Fe-0.9Zr alloy are plotted in Fig. 11(a). The tensile properties of YS, UTS, and El are extracted from these curves. For the as-built sample, the YS, UTS, and El are 395 ± 27 MPa, 560 ± 26 MPa, and 4.3 ± 1.3%, respectively. After aging treatments, the YS and UTS generally decrease, while the El increases. Aging at 300 °C for 6 h reduces the YS by 6% to 370 ± 13 MPa and the UTS by 9% to 511 ± 14 MPa, while increasing the El by 69% to 7.2 ± 1.5%. After 400 °C aging for 6 h, the YS further declines to 351 ± 14 MPa, the UTS reduces to 436 ± 8 MPa, while the El improves to 9.6 ± 0.9%. The strength reduction after aging is mainly associated with intermetallic coarsening, which is limited after 300 °C aging but becomes evident after 400 °C aging compared with the as-printed state, see Fig. S4. A direct comparison of the tensile properties of the present LPBF Al-6.5Ni-1.4Fe-0.9Zr alloy with other Al-Ni based alloys fabricated by multiple methods is listed in Table 2. The Al-6.5Ni-1.4Fe-0.9Zr alloy in this work possesses enhanced mechanical properties and a better balance of strength and ductility compared to the other Al-Ni based alloys. To enable a more direct strength-ductility comparison in the as-printed condition, Fig. 11(c) plots YS against tensile elongation for a range of LPBF eutectic Al alloys, including Al-Ni, Al-Ce, and Al-La based systems. The as-printed Al-6.5Ni-1.4Fe-0.9Zr alloy reaches a YS of ~395 MPa, positioning it at the high-strength end of the dataset. Notably, this value is higher than those reported for Sc-containing LPBF Al-5.9Ni-0.3Sc (~320 MPa) [32], Al-5.6Ni-0.7Sc-0.1Zr (~368 MPa)

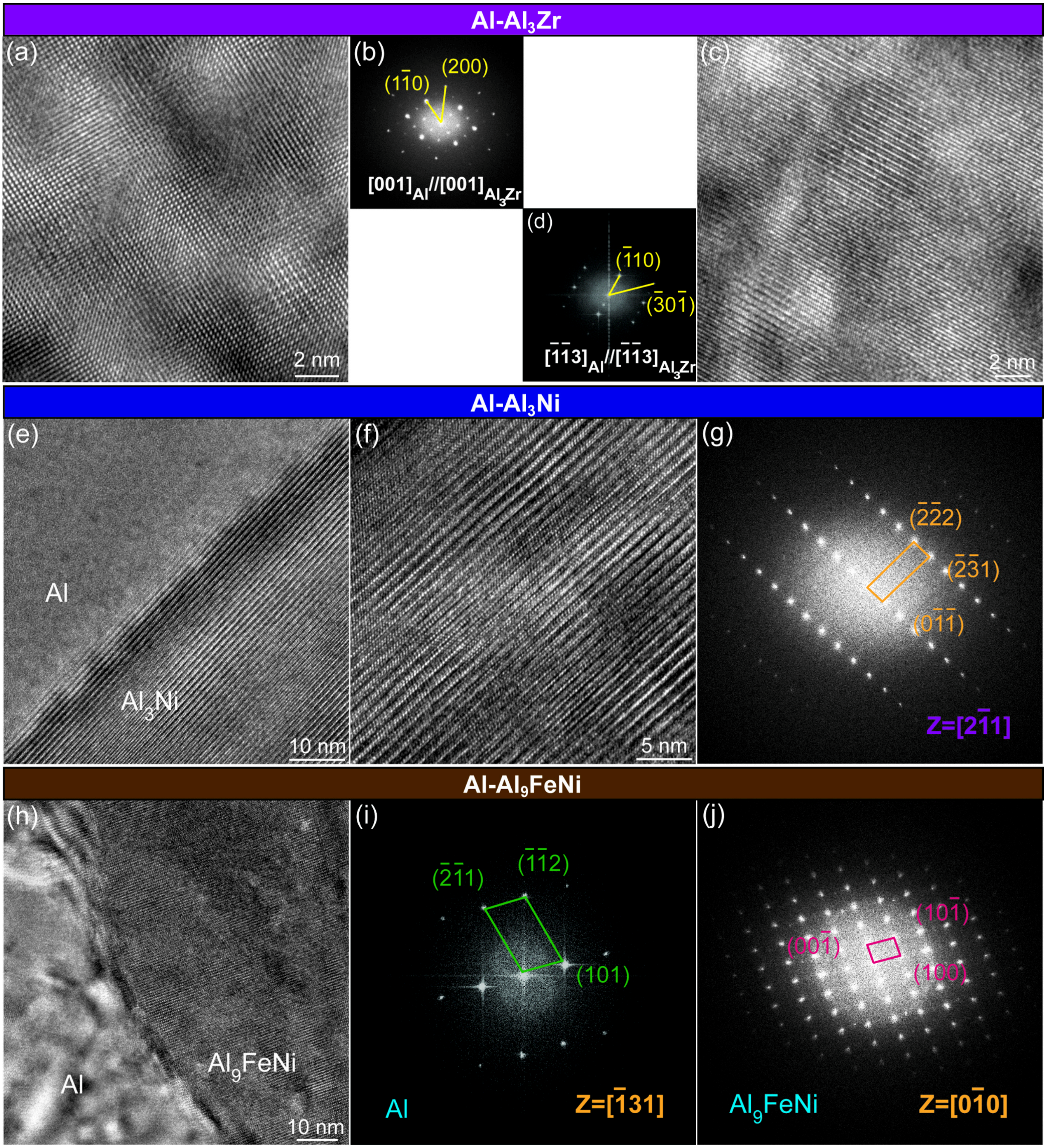

Fig. 8. TEM characterization of the sample aged at 400 °C for 100 h. HRTEM images and corresponding FFT showing $[001]_{Al}//[001]_{Al_3Zr}$ (a, b) and $[\overline{11}\,3]_{Al}//[\overline{11}3]_{Al_3Zr}$ (c, d) coherent orientations. (e) HRTEM image of Al/Al_3Ni interface, (f) enlarged view of Al_3Ni, and (g) corresponding FFT of (e). (h) HRTEM image of Al/Al_9FeNi interface and corresponding FFT for Al (i) and Al_9FeNi (j).

[39], and Al-10Ce-0.4Sc-0.2Zr [40] benchmark, highlighting that the present alloy design achieves competitive strength while avoiding reliance on costly Sc additions.

The engineering stress–strain responses at 25, 200, 300 and 350 °C (Fig. 11(b)) reveal a strong temperature dependence of the load-bearing capacity. Using the room-temperature UTS of ~560 MPa as the baseline, the alloy retains 353.9 MPa at 200 °C, 194.9 MPa at 300 °C, and 100.8 MPa at 350 °C. When benchmarked against other eutectic Al alloys processed by AM, the present alloy shows competitive high-temperature strength among the Sc-free alloys as listed in Table 3. The UTS of 194.9 MPa at 300 °C exceeds most reported Sc-free Al-Ni and Al-Ce alloys, such as LPBF Al-5.6Ni-0.9Ti-0.9Zr (134.3 MPa) [49], LPBF Al-8.6Cu-0.5Mn-0.9Zr (~150 MPa) [51], WAAM Al-15Ce-3 Mg (~86.1 MPa) [52], and LPBF Al-10.5Ce-3.1Ni-1.2Mn (~155 MPa) [53], while remaining

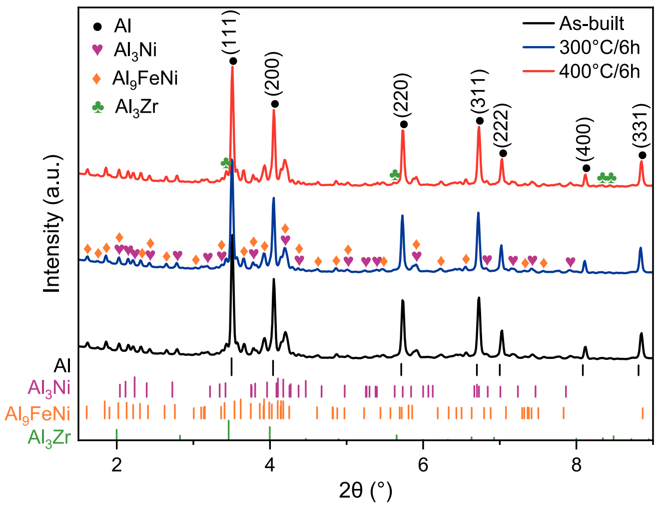

Fig. 9. Synchrotron XRD patterns of as-built and heat-treated Al-6.5Ni-1.4Fe-0.9Zr specimens.

comparable to LPBF Al-10Ce (194 MPa) [40]. However, the UTS at 300 °C remains below that of Sc-modified counterparts: LPBF Al-5.6Ni-0.7Sc-0.1Zr reaches 212 MPa [39] and LPBF Al-10Ce-0.4Sc-0.2Zr achieves 233 MPa [40]. The better high-temperature strength of Sc-containing alloys is attributed to Sc segregation at the Al-Ni cell wall interface, which can reduce the interfacial energy between the intermetallic phase and the Al matrix, thereby lowering the thermodynamic driving force for coarsening. Despite this gap, the combination of strong room-temperature strength and high-temperature performance exceeding most Sc-free AM eutectic alloys makes the Al-Ni-Fe-Zr composition a promising, cost-effective candidate for heat-resistant applications.

To better understand the fracture mechanism, Fig. 12 displays the fracture morphology for the as-built and aged specimens. All fracture surfaces exhibit the same spherical gas-driven pores, characterized by a round shape, smooth inner surface, and fine size. Unfortunately, gas-driven pores are an intrinsic feature of AM technologies, which is difficult to eliminate by processing parameter optimization and post treatment [55]. Many rugged and jagged edges are observed in the as-printed sample (Fig. 12(a, b)), suggesting a brittle fracture behavior. Irregular ridges and big voids are distributed in the fractured sample

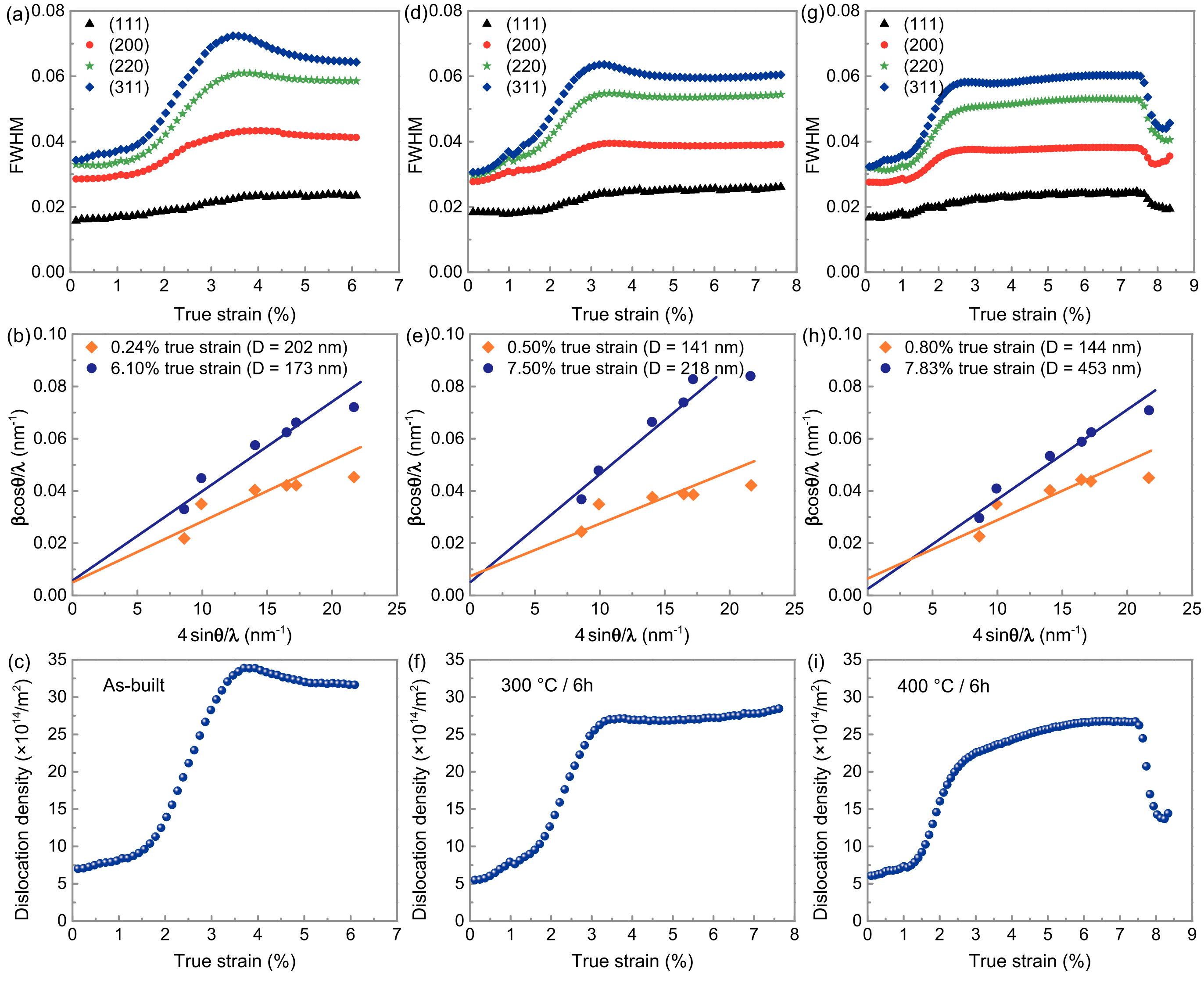

Fig. 10. Dislocation densities of the α-Al matrix derived from the SXRD patterns and Williamson-Hall method for the specimens of as-built (a–c), 300 °C/6h annealed (d–f) and 400 °C/6h annealed (g–i). (a, d, g) The raw FWHM of the Al phase; (b, e, h) Representative results of Williamson-Hall plots at various true strains; (c, f, i) Dislocation densities.

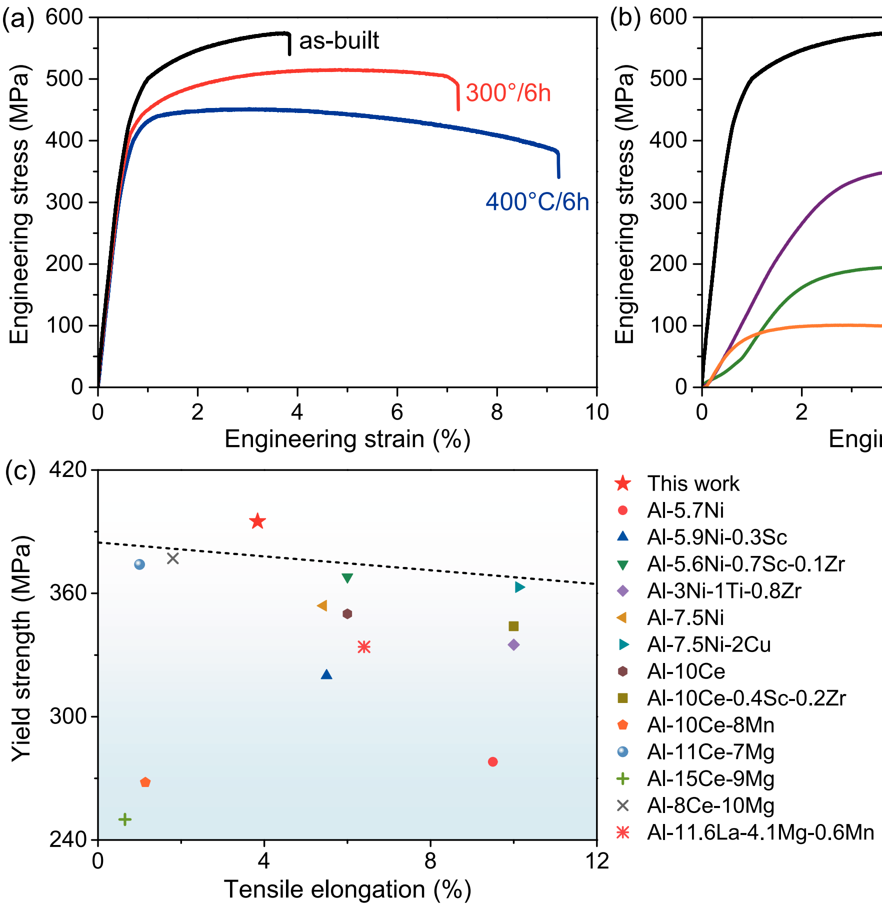

Fig. 11. (a) Room-temperature tensile curves of the as-printed and aged specimens, (b) high-temperature tensile curves, and (c) comparison of YS and tensile elongation tested at room-temperature for the Al-6.5Ni-1.4Fe-0.9Zr alloy and other LPBF fabricated eutectic Al alloys, including Al-5.7Ni [15], Al-5.9Ni-0.3Sc [32], Al-5.6Ni-0.7Sc-0.1Zr [39], Al-3Ni-1Ti-0.8Zr [41], Al-7.5Ni [42], Al-7.5Ni-2Cu [42], Al-10Ce [40], Al-10Ce-0.4Sc-0.2Zr [40], Al-10Ce-8Mn [43], Al-11Ce-7 Mg [44], Al-15Ce-9 Mg [44], Al-8Ce-10 Mg [45], and Al-11.6La-4.1 Mg-0.6Mn [46] alloys.

after 300 °C aging for 6 h (Fig. 12(c)). However, a high number of fine dimples are found in Fig. 12(d). These features indicate a combination of brittle and ductile fracture behavior. Aging at 400 °C for 6 h results in a smoother fracture surface (Fig. 12(e)). Moreover, there are lots of precipitated Al_9FeNi particles (Fig. 12(f and g)), contributing to enhanced ductility. Macroscopically, the last tensile failed sample presents a necking region at the middle part (Fig. 12(h)). Aging treatment in Al alloys significantly enhances tensile properties through precipitation hardening, which increases strength and hardness. However, under tensile stress, these hardening phases can cause stress concentrations, leading to localized plastic deformation and necking. The fracture morphology in the necking region typically exhibits cup-cone fracture with deep dimples. These dimples, characteristic of ductile fracture, form due to the coalescence of micro-voids [56,57].

4. Discussion

4.1. Mechanism of cellular structure formation

In the LPBF Al-6.5Ni-1.4Fe-0.9Zr alloy, the formation of a cellular eutectic structure, with Al_3Ni forming the cell walls around the α-Al phase, is primarily driven by rapid solidification conditions. The high cooling rates characteristic of LPBF create a steep thermal gradient (G) and a fast solidification rate (V), which are essential for stabilizing the solid–liquid interface and promoting the development of a fine microstructure.

According to the Jackson-Hunt model [58], the cellular spacing (λ) within the eutectic structure is inversely proportional to the product of the thermal gradient and the solidification rate, as expressed by the following equation:

$$\lambda \propto (G \cdot V)^{-\frac{1}{2}} \tag{5}$$

This relationship suggests that as the cooling rate increases, the cellular spacing decreases, resulting in a more refined cellular structure. The high cooling rates in LPBF not only produce finer structures but also improve the uniformity of the cellular eutectic phases.

Furthermore, the distribution and concentration of solute elements such as Ni, Fe, and Zr during solidification significantly affect the stability of the solid–liquid interface. Due to the differing solid–liquid partition coefficients of these elements, solute enrichment occurs at the solidification front. This enrichment results in constitutional supercooling, which stabilizes the interface under rapid cooling conditions and promotes the growth of cellular structures.

The non-equilibrium solidification effects, particularly the Gibbs-Thomson effect, are crucial in further refining the microstructure. The Gibbs-Thomson effect describes the impact of interface curvature on undercooling, as expressed by the following equation [59,60]:

$$\Delta T = \frac{2\gamma_{SL}}{r\Delta S_f} \tag{6}$$

where ΔT represents the undercooling, γ_{SL} is the solid–liquid interface energy, r is the curvature radius, and ΔS_f is the entropy change upon solidification. In the context of LPBF, the high cooling rates lead to significant undercooling, which, in combination with the small

Table 2
Comparison of room-temperature tensile properties of the present Al-6.5Ni-1.4Fe-0.9Zr alloy with other Al-Ni based alloys (WAAM: wire arc additive manufacturing, LMD: laser metal deposition).

Alloy (wt.%)	Process	YS (MPa)	UTS (MPa)	El (%)	Ref.
Al-6.5Ni-1.4Fe-0.9Zr	LPBF	395 ± 27	560 ± 26	4.3 ± 1.3	This work
	LPBF + 300 °C/6h	370 ± 13	511 ± 14	7.2 ± 1.5	This work
	LPBF + 400 °C/6h	351 ± 14	436 ± 8	9.6 ± 0.9	This work
Al-6.5Ni	Cast	200 ± 9	308 ± 14	~14	[25]
Al-6.5Ni-0.5Zr	Cast	255 ± 13	350 ± 11	~12	[25]
Al-5.7Ni	LPBF	278 ± 5	407 ± 6	9.5 ± 0.3	[15]
Al-5.9Ni-0.3Sc	LPBF	320	445	~5.5	[32]
Al-4.3Ni-2.8 Mg	WAAM	141.4 ± 9.8	318.7 ± 2.3	14.4 ± 3.0	[47]
Al-3Ni-1Ti-0.8Zr	LPBF	266 ± 1	331 ± 9	17 ± 1	[41]
	LPBF + 300 °C/4h	335 ± 10	345 ± 7	10 ± 3	[41]
Al-4Ni-2Cu-1.3Fe-0.7Mn-0.7Zr-0.5Cr-0.15Sc	LPBF	578	725	3.1	[48]
	LPBF + 530 °C/1h	373	537	10.3	[48]
Al-5.6Ni-0.9Ti-0.9Zr	LPBF	421.7	480.4	~8.5	[49]
	LPBF + 325 °C/12 h	494	550.7	~10	[49]
Al-7.5Ni	LMD	185 ± 11	268 ± 15	13.4 ± 1.9%	[50]
Al-7.5Ni	LPBF	354 ± 1.2	484 ± 0.8	5.4 ± 0.69	[42]
Al-7.5Ni-2.0Cu	LPBF	363 ± 0.7	545 ± 2.0	10.1 ± 0.34	[42]

Table 3
Comparison of high-temperature UTS retention between the Al-6.5Ni-1.4Fe-0.9Zr alloy and other eutectic Al alloys.

Alloy (wt.%)	Process	Temperature (°C)	UTS (MPa)	Ref.
Al-6.5Ni-1.4Fe-0.9Zr	LPBF	200	353.9	This work
		300	194.9	This work
		350	100.8	This work
Al-5.6Ni-0.9Ti-0.9Zr	LPBF	200	350.2	[49]
		250	264.6	[49]
		300	134.3	[49]
Al-5.6Ni-0.7Sc-0.1Zr	LPBF	200	394	[39]
		250	337	[39]
		300	212	[39]
Al-8.6Cu-0.5Mn-0.9Zr	LPBF	200	~275	[51]
		300	~150	[51]
Al-4.5Mn-1Mg-0.8Sc-0.6Zr	LPBF	200	361	[54]
		250	240	[54]
		300	136	[54]
Al-15Ce-3Mg	WAAM	220	132.7 ± 3.6	[52]
		250	121.9 ± 2	[52]
		300	86.1 ± 2	[52]
Al-10.5Ce-3.1Ni-1.2Mn	LPBF + 450 °C/2h	300	~155	[53]
		400	~100	[53]
Al-10Ce	LPBF	300	194	[40]
		400	80	[40]
Al-10Ce-0.4Sc-0.2Zr	LPBF	300	233	[40]
		400	131	[40]

curvature radius at the cellular interfaces, further refines the cellular eutectic structure.

The solidification mechanisms ensure that the Al-6.5Ni-1.4Fe-0.9Zr alloy produced by LPBF develops a highly refined and stable cellular eutectic microstructure, characterized by finely and uniformly distributed Al_3Ni phases within the Al matrix. As seen in Fig. 3(e), the cell diameter of LPBF Al-6.5Ni-1.4Fe-0.9Zr alloy is approximately 300 nm, which is in the same submicron range as the as-printed cellular diameters reported for other LPBF Al alloys, including ~500 nm in LPBF AlSi10Mg with nano TiB_2 [61] and ~350 nm in LPBF Al-9Cu-6Ce [62] alloys. The refined microstructure contributes to enhanced mechanical strength and thermal stability, making the alloy highly suitable for high-temperature applications where material heat resistance is critical.

4.2. Ostwald ripening and thermal stability

Most cast and wrought Al alloys are unsuitable for structural applications above 200 °C due to the instability of their strengthening precipitates, which tend to coarsen and dissolve at elevated temperatures [63]. The as-built Al-6.5Ni-1.4Fe-0.9Zr alloy demonstrates excellent heat resistance, with only a slight decrease in hardness after 100 h of thermal exposure at 250–350 °C (see Fig. 6). Compared to the LPBF Al-5.9Ni-0.3Sc alloy studied by Ding et al. [32], which exhibited a significant reduction in hardness after just 15 h at 350 °C and 400 °C due to precipitate coarsening, the Al-6.5Ni-1.4Fe-0.9Zr alloy maintains its hardness more effectively. Similarly, Yang et al. [40] observed a marked decline in hardness in an LPBF Al-10Ce alloy following prolonged high-temperature exposure at 350 °C. However, the addition of Sc and Zr to the LPBF Al-10Ce-0.4Sc-0.2Zr alloy improves heat resistance under exposure to 400 °C, attributed to the dispersive $Al_3(Sc, Zr)$ nanoparticles and the segregation of Sc and Zr at the $Al/Al_{11}Ce_3$ interface. When subjected to 400 °C thermal exposure, the microhardness of the LPBF Al-6.5Ni-1.4Fe-0.9Zr alloy follows three distinct stages: an initial decrease within the first hour, a plateau, and a subsequent drop after 16 h. These changes can be attributed to the following mechanisms: (1) Dislocation annihilation occurs during the initial 1 h, leading to a reduction in dislocation density and a corresponding decrease in hardness. (2) The formation of Al_3Zr precipitates, which are coherently oriented with the Al matrix as observed in HRTEM images (Fig. 8(a and c)) and FFT patterns (Fig. 8(b and d)), helps maintain microhardness at prolonged exposure time. (3) Coarsening of Al_3Ni particles, which becomes prominent after 16 h at 400 °C, results in a rapid decline in microhardness to 121.1 HV after 100 h as the cellular structure dissolves into larger, scattered particles (Fig. 7).

The precipitate growth and dissolution are significantly influenced by the kinetics of Ostwald ripening [64]. This process involves the preferential growth of larger phase domains at the expense of smaller ones, a phenomenon driven by the smaller surface-to-volume ratios of the larger domains. LSW coarsening theory quantitatively describes the Ostwald ripening and predicts the time-dependent average particle radius [65]:

$$\langle R(t)\rangle^3 - \langle R(0)\rangle^3 = Kt \tag{7}$$

where $\langle R(t)\rangle$ is the mean diameter at aging time t and K is the coarsening rate constant. Based on the particle size measurements from Fig. 3(e, f), Fig. S4(c, d), Fig. S5 and Fig. 7(a, b), the average particle diameter increases from ~35 nm in the as-built condition to ~64 nm at 6 h, ~109 nm at 64 h, and ~120 nm at 100 h upon thermal exposure at 400 °C. The size evolution exhibits a clear two-stage behavior: faster coarsening in the early stage is attributed to rapid supersaturation depletion, followed by progressively slower growth as the ripening process becomes increasingly diffusion-limited. An LSW-based analysis reveals coarsening rates of ~10.2 nm^3/s (0–6 h), ~4.9 nm^3/s (6–64 h), and ~3.3 nm^3/s (64–100 h), with an average of ~6.1 ± 3.5 nm^3/s over 0–100 h. This coarsening rate is notably lower than those reported for other

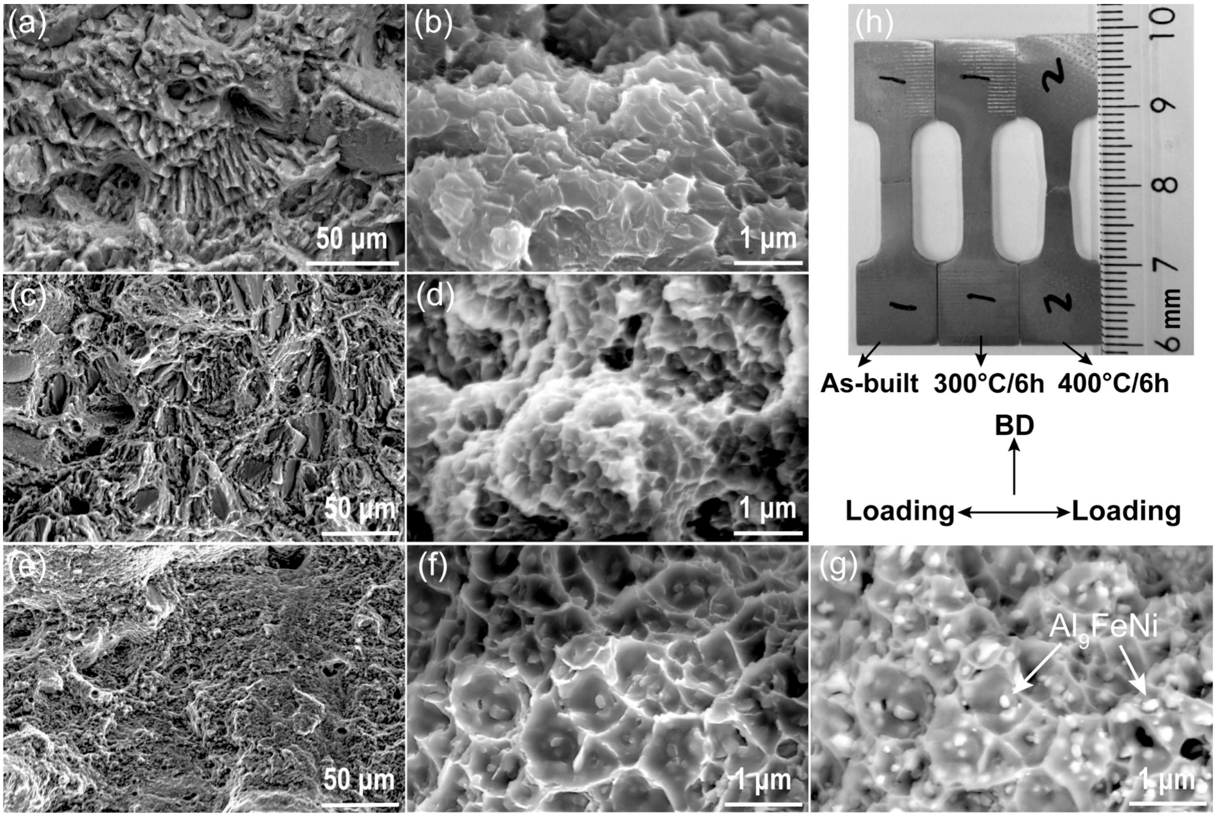

Fig. 12. SEM micrographs of fracture surfaces of (a, b) as-built, (c, d) 300 °C/6h aging, and (e, f) 400 °C/6h aging samples. (g) Corresponding BSE image of (f). (h) Top views of tensile failed samples.

strengthening phases in Al alloys, such as Al_2Cu in cast Al-4.8Cu alloy [66] and Si in LPBF Al-12Si alloy [67].

The low coarsening rate of the Al-6.5Ni-1.4Fe-0.9Zr alloy can be attributed to a combination of critical factors. The alloying elements of Ni, Fe, and Zr form stable dispersoids within the Al matrix, remaining thermodynamically stable at elevated temperatures. The low diffusivity of Ni in Al at 400 °C ($D_{Ni/Al} = 2.05 \times 10^{-15}$ m^2/s [68]) effectively restricts diffusion-driven coarsening of the dispersoid phases. Meanwhile, the low solubility of Ni in Al (0.023 at.% [69]) minimizes the dissolution of these dispersoids, maintaining a fine microstructure over time. Note that Zr significantly enhances the coarsening resistance by segregating at the α-Al/Al_3Ni interface, which reduces interface energy and inhibits atomic migration [25]. Zr segregation prevents the breaking or spheroidization of Al-Al_3Ni network. Stable phase formation, low diffusivity, and enhanced interface stability work synergistically, making the LPBF Al-6.5Ni-1.4Fe-0.9Zr alloy a strong candidate for applications demanding long-term thermal stability.

Table 4
Overview of the constants applied in this study for calculating the different factors influencing YS.

Symbols	Meanings	Values	Ref.
σ_0	Friction stress of Al	11 MPa	[70]
k	Strengthening coefficient	0.06 MPa·$m^{1/2}$	[71]
d	Average cell diameter	300 nm	This work
M	Taylor factor	3.06	[18]
v	Poisson's ratio of Al	0.347	[72]
$w = 5b$	Interaction force parameter	1.430 nm	[18]
b	Burgers vector of Al	0.286 nm	[73]
G	Shear modulus of Al	25.4 GPa	[74]
ε_{Ni}	Misfit strain for Ni	−3.13 ± 0.06%	[18]
ε_{Fe}	Misfit strain for Fe	−4.52 ± 0.08%	[18]
ε_{Zr}	Misfit strain for Zr	1.23 ± 0.12%	[18]
α	Constant	0.24	[75]
ρ	Dislocation density	6.9×10^{14} m^{-2}	This work

4.3. Strengthening contribution

Table 2 lists the excellent YS of 395 MPa observed in the as-built Al-6.5Ni-1.4Fe-0.9Zr alloy compared to other Al-Ni alloys, attributed to its fine cellular structure. The strengthening mechanisms in the as-printed condition are discussed to evaluate the contributions and identify the predominant factors. Notably, precipitation hardening from the Al_3Zr phase in the as-built sample is negligible since no aging treatment was conducted. The rapid solidification of the LPBF process traps most Zr elements in solid solution, suppressing precipitate formation. Table 4 provides a summary explaining the variables used to estimate the YS. Overall, the primary factors contributing to the YS of the as-built alloy are: (1) grain boundary strengthening, (2) solid solution strengthening, and (3) dislocation strengthening, and (4) Orowan strengthening, see Table 5.

LPBF offers a significant advantage in refining the fine cell structure, generating a dense network that effectively impedes dislocation movement and propagation, resulting in greater material strength [76]. The Hall-Petch equation typically characterizes the grain-boundary strengthening mechanism [77]:

$$\Delta\sigma_{cell} = \sigma_0 + \frac{k}{\sqrt{d}} \tag{8}$$

Table 5
Main YS contributions in the as-printed Al-6.5Ni-1.4Fe-0.9Zr alloy (Unit: Mpa).

Condition	$\Delta\sigma_{cell}$	$\Delta\sigma_{ss}$	$\Delta\sigma_{dis}$	$\Delta\sigma_{Oro}$	Exp.
As-built	119.4	38.9	139.8	100.8	395

where σ_0 is the friction stress of Al, k is the strengthening coefficient, and d is the average cell diameter. Based on Fig. 3(e) and Fig. 5(b–d), which shows an equivalent cell size of 300 nm, the contribution from cell boundaries is estimated to be ~119.4 MPa.

Solid-solution strengthening occurs when alloying elements are introduced into a metal matrix as solute atoms. These solute atoms, differing in size or shear modulus from the matrix atoms, generate localized strain fields. These fields interact with dislocations, hindering their movement and thereby strengthening the material [78,79]. Uesugi et al. [18] presented the application of the misfit strains to the estimation of increasing yield strength due to the solid solution strengthening:

$$\Delta\sigma_{ss} = M\left(\frac{3}{8}\right)^{2/3}\left(\frac{1+\nu}{1-\nu}\right)^{4/3}\left(\frac{w}{b}\right)^{1/3} G \times \sum_i |\varepsilon_i|^{4/3} c_i^{\,2/3} \tag{9}$$

where M is the Taylor factor, ν is the Poisson's ratio of Al, w is the interaction force parameter, b is the Burgers vector of Al, G is the Shear modulus of Al, ε_i the misfit strain for the solute i (Ni and Fe), and c_i the concentration of solute i in solid solution. According to TEM-EDS results, the matrix contains Ni, Fe and Zr solutes at concentrations of 0.05, 0.04 and 0.35 at%, respectively. The $\Delta\sigma_{ss}$ is calculated to be ~38.9 MPa.

During LPBF, the steep thermal gradients and rapid cooling generate significant thermal strains and residual stresses, which promote a high density of dislocations in the as-built microstructure. The contribution from dislocation strengthening was estimated using the Bailey-Hirsch relationship [80,81]:

$\Delta\sigma_{dis} = M\alpha Gb\rho^{1/2}$(10).where α is a constant, ρ denotes the dislocation density. Based on the synchrotron XRD results in Fig. 10(c), the initial dislocation density of the as-built sample before tensile loading is ~6.9×10^{14} m^{-2}, corresponding to a contribution of ~139.8 MPa.

The strengthening effect associated with non-shearable Al_3Ni/Al_9FeNi particles is treated separately via the Orowan bypass mechanism. While this mechanisms can be coupled in practice with the dislocation strengthening, the present decomposition adopts a first-order separation to quantify their relative contributions. For the Al_3Ni and Al_9FeNi intermetallic particles in the present alloy, the Orowan contribution is calculated using the following equation [40,79]:

$$\Delta\sigma_{Oro} = M\frac{0.4Gb}{\pi\sqrt{1-\nu}}\frac{ln\left[\frac{2\bullet\sqrt{2/3}\bullet R}{b}\right]}{\lambda} \tag{11}$$

$$\lambda = \left(\sqrt{\frac{3\pi}{4f}} - 1.64\right)R \tag{12}$$

where R denotes the mean particle radius (~18 nm), λ represents the edge-to-edge interparticle spacing, and f is particle volume fraction. With the particle volume fraction determined by TEM to be ~2.1%, the estimated Orowan strengthening increment is ~100.8 MPa.

After aging at 300 °C for 6 h, the yield strength decreases to 370 MPa and drops further to 351 MPa after aging at 400 °C for 6 h. The strengthening balance shifts during aging compared with the as-built state. The fine eutectic cell network that provides a major share of the as-built strengthening becomes less effective because the cellular boundaries are largely disrupted and fragmented during aging, while grain growth remains limited. Under this circumstance, the characteristic length scale for the Hall-Petch term should more appropriately be taken as the grain size rather than the cell diameter. During aging, Zr is expected to precipitate largely out of the supersaturated α-Al matrix, and the solubility of Ni and Fe in α-Al is intrinsically very limited. As a result, solid solution strengthening in the aged condition is negligible. Synchrotron XRD further indicates partial recovery after heat treatment, accompanied by a reduced dislocation density, thereby weakening the dislocation strengthening contribution. The main Orowan obstacles remain the non-shearable Al_3Ni/Al_9FeNi intermetallics, and aging does not introduce a large number of new intermetallic particles, while coarsening increases the effective spacing and reduces the Orowan increment. Meanwhile, $L1_2$-Al_3Zr nanoprecipitates introduce additional strengthening through coherency and modulus mismatch, see Supplementary Materials for detailed analyses. As summarized in Fig. S6, the Al_3Zr-related contribution is estimated to be comparable for 300 °C/6h and 400 °C/6h because Al_3Zr shows limited coarsening even after 100 h exposure at 400 °C, and it accounts for ~38% of the total estimated strengthening in the aged state. Overall, the added Al_3Zr strengthening is insufficient to offset the concurrent reductions in cell boundary, dislocation, and Orowan strengthening, which explains why the YS does not exceed the as-printed value after aging.

5. Conclusions

This study successfully demonstrates the design and fabrication of a high-strength, heat-resistant LPBF Al-6.5Ni-1.4Fe-0.9Zr near-eutectic alloy. The following conclusions can be drawn from the research:

1. The novel Al-6.5Ni-1.4Fe-0.9Zr alloy was designed with a near-eutectic composition to optimize LPBF processability and reduce hot tearing susceptibility. The carefully balanced eutectic composition allowed for crack-free manufacturing, resulting in a refined cellular microstructure (~300 nm) with uniformly distributed Al_3Ni phases as well as scattered Al_9FeNi phases. The rapid cooling rate in LPBF contributes to this microstructure by promoting cellular growth, effectively enhancing both strength and ductility at the microscale level
2. The as-built alloy shows a YS of 395 MPa, UTS of 560 MPa, and El of 4.3%. EBSD analysis indicates an ultrafine grain distribution in the as-built state, with an average grain size of 3.4 μm perpendicular and 4.3 μm along the BD, reducing anisotropy through Zr-induced nucleation. Aging treatment at 300 °C for 6 h decreases the YS to 370 MPa, as the reductions in cell boundary, dislocation and Orowan strengthening outweigh the added Al_3Zr strengthening contribution. After 400 °C aging for 100 h, the cellular structure decomposes into globular particles with an average diameter of ~ 120 nm
3. *In situ* synchrotron XRD analysis revealed that dislocation density significantly increases under tensile strain, enhancing mechanical strength through strain hardening. Aging treatments partially annihilate dislocations and foster interactions with precipitates, redistributing stress and enhancing ductility. This thermally moderated recovery optimizes substructure stability, producing a favorable balance of strength and ductility
4. The alloy maintains high hardness and microstructural integrity under thermal exposure at 250–350 °C for 100 h, demonstrating superior resistance to coarsening. After 400 °C aging for 100 h, a noticeable decline in hardness is observed due to the coarsening of Al_3Ni phases, but the presence of nanosized $L1_2$-Al_3Zr particles, mitigates this effect, maintaining a low coarsening rate of 6.1 nm^3/s
5. This work shows that high strength retention and sustained high-temperature stability in LPBF Al alloys can be achieved by pairing a eutectic cellular microstructure with coherency stabilised interfaces, which together suppress thermally driven microstructural coarsening. It offers a practical strategy for the design of high-strength and heat-resistant Al alloys for thermally demanding service

CRediT authorship contribution statement

Feng Li: Writing – original draft, Visualization, Validation, Methodology, Investigation, Funding acquisition, Formal analysis, Data curation, Conceptualization. **Wei Zhang:** Writing – review & editing,

Validation, Investigation, Formal analysis. **Jiajia Shen:** Software, Formal analysis. **J.P. Oliveira:** Resources, Funding acquisition. **Dan Li:** Software, Formal analysis. **Chao Chen:** Validation, Resources. **Shaochuan Feng:** Writing – review & editing, Validation, Investigation. **Norbert Schell:** Resources, Funding acquisition. **Bart J. Kooi:** Writing – review & editing, Supervision. **Yutao Pei:** Writing – review & editing, Validation, Supervision, Project administration, Methodology, Investigation, Funding acquisition, Conceptualization.

Declaration of competing interest

The authors declare that they have no known competing financial interests or personal relationships that could have appeared to influence the work reported in this paper.

Acknowledgements

We acknowledge the financial support by Samenwerkingsverband Noord-Nederland (SNN) within the program “3D Print Kompas 2030”. FL acknowledges the China Scholarship Council for his Ph.D. Scholarship (CSC, No. 202206370054). JPO and JS acknowledge financial support provided by Fundação para a Ciência e a Tecnologia (FCT-MCTES) through project UID/00667/2020 (UNIDEMI). JPO also acknowledges support from national funds awarded by FCT - Fundação para a Ciência e a Tecnologia, I.P., within the framework of the Associate Laboratory Institute of Nanostructures, Nanomodelling and Nanofabrication – i3N, under projects LA/P/0037/2020, UIDP/50025/2020, and UIDB/50025/2020. The authors gratefully acknowledge DESY (Hamburg, Germany), a member of the Helmholtz Association HGF, for providing access to synchrotron facilities and granting beamtime under proposal I-20210899 EC. This research was partially supported by the CALIPSOplus project (Grant Agreement 730872) within the EU Framework Programme for Research and Innovation HORIZON 2020.

Appendix A. Supplementary data

Supplementary data to this article can be found online at https://doi.org/10.1016/j.matdes.2026.115997.

Data availability

The data that support the findings of this study are openly available in figshare at https://doi.org/10.6084/m9.figshare.30920684.

References

[1] J.H. Martin, B.D. Yahata, J.M. Hundley, J.A. Mayer, T.A. Schaedler, T.M. Pollock, 3D printing of high-strength aluminium alloys, Nature 549 (2017) 365–369, https://doi.org/10.1038/nature23894.

[2] N.T. Aboulkhair, M. Simonelli, L. Parry, I. Ashcroft, C. Tuck, R. Hague, 3D printing of aluminium alloys: additive manufacturing of aluminium alloys using selective laser melting, Prog. Mater Sci. 106 (2019) 100578, https://doi.org/10.1016/j.pmatsci.2019.100578.

[3] H. Xue, C. Yang, F. De Geuser, P. Zhang, J. Zhang, B. Chen, F. Liu, Y. Peng, J. Bian, G. Liu, A. Deschamps, J. Sun, Highly stable coherent nanoprecipitates via diffusion-dominated solute uptake and interstitial ordering, Nat. Mater. 22 (2023) 434–441, https://doi.org/10.1038/s41563-022-01420-0.

[4] N. Takata, K. Minamihama, T. Miyawaki, Y. Cheng, Y. Xu, W. Wang, D. Kim, A. Suzuki, M. Kobashi, M. Kato, Design of high-performance sustainable aluminum alloy series for laser additive manufacturing, Nat. Commun. 16 (2025) 11105, https://doi.org/10.1038/s41467-025-67281-8.

[5] C. Hao, Y. Sui, Y. Yuan, P. Li, H. Jin, A. Jiang, Composition optimization design and high temperature mechanical properties of cast heat-resistant aluminum alloy via machine learning, Mater. Des. 250 (2025) 113587, https://doi.org/10.1016/j.matdes.2025.113587.

[6] I.M. Kusoglu, B. Gökce, S. Barcikowski, Research trends in laser powder bed fusion of Al alloys within the last decade, Addit. Manuf. 36 (2020) 101489, https://doi.org/10.1016/j.addma.2020.101489.

[7] F. Li, Z. Li, C. Tang, L. Zhang, Q. Tan, C. Chen, M. Zhang, K. Zhou, Design high-strength Al-Mg-Si alloy fabricated by laser powder bed fusion: cracking suppression and strengthening mechanism, Mater. Sci. Eng. A 864 (2023) 144591, https://doi.org/10.1016/j.msea.2023.144591.

[8] F. Li, T. Zhang, Y. Wu, C. Chen, K. Zhou, Microstructure, mechanical properties, and crack formation of aluminum alloy 6063 produced via laser powder bed fusion, J. Mater. Sci. 57 (2022) 9631–9645, https://doi.org/10.1007/s10853-022-06993-4.

[9] S. Pauly, P. Wang, U. Kühn, K. Kosiba, Experimental determination of cooling rates in selectively laser-melted eutectic Al-33Cu, Addit. Manuf. 22 (2018) 753–757, https://doi.org/10.1016/j.addma.2018.05.034.

[10] N.E. Uzan, R. Shneck, O. Yeheskel, N. Frage, High-temperature mechanical properties of AlSi10Mg specimens fabricated by additive manufacturing using selective laser melting technologies (AM-SLM), Addit. Manuf. 24 (2018) 257–263, https://doi.org/10.1016/j.addma.2018.09.033.

[11] J. Li, M. Zhang, Heat resistance TiB$_2$/AlSi10Mg alloy prepared via laser powder bed fusion: New insights into microstructure evolution and medium temperature mechanical properties at 300 °C, Mater. Sci. Eng. A 951 (2025) 149625, https://doi.org/10.1016/j.msea.2025.149625.

[12] P. He, H. Kong, Q. Liu, M. Ferry, J.J. Kruzic, X. Li, Elevated temperature mechanical properties of TiCN reinforced AlSi10Mg fabricated by laser powder bed fusion additive manufacturing, Mater. Sci. Eng. A 811 (2021) 141025, https://doi.org/10.1016/j.msea.2021.141025.

[13] J.-X. Sun, G.-M. Sun, A.W. Shah, W.-F. Li, K. Wang, S.-X. Jin, B.-B. Wan, D.-X. Zeng, D.-C. Zeng, Wire-powder-arc additive manufacturing of alternating graded TiC and B$_4$C particles reinforced aluminum matrix composite structures, Virtual Phys. Prototyp. 20 (2025) e2560021, https://doi.org/10.1080/17452759.2025.2560021.

[14] O.H. Famodimu, M. Stanford, C.F. Oduoza, L. Zhang, Effect of process parameters on the density and porosity of laser melted AlSi10Mg/SiC metal matrix composite, Front. Mech. Eng. 13 (2018) 520–527, https://doi.org/10.1007/s11465-018-0521-y.

[15] J. Deng, C. Chen, X. Liu, Y. Li, K. Zhou, S. Guo, A high-strength heat-resistant Al-5.7Ni eutectic alloy with spherical Al$_3$Ni nano-particles by selective laser melting, Scr. Mater. 203 (2021) 114034, https://doi.org/10.1016/j.scriptamat.2021.114034.

[16] A. Plotkowski, O. Rios, N. Sridharan, Z. Sims, K. Unocic, R.T. Ott, R.R. Dehoff, S. S. Babu, Evaluation of an Al-Ce alloy for laser additive manufacturing, Acta Mater. 126 (2017) 507–519, https://doi.org/10.1016/j.actamat.2016.12.065.

[17] Y. Fan, M.M. Makhlouf, The Al-Al$_3$Ni eutectic reaction: crystallography and mechanism of formation, Metall. Mater. Trans. A 46 (2015) 3808–3812, https://doi.org/10.1007/s11661-015-3051-9.

[18] T. Uesugi, K. Higashi, First-principles studies on lattice constants and local lattice distortions in solid solution aluminum alloys, Comput. Mater. Sci. 67 (2013) 1–10, https://doi.org/10.1016/j.commatsci.2012.08.037.

[19] T. Mukai, S. Suresh, K. Kita, H. Sasaki, N. Kobayashi, K. Higashi, A. Inoue, Nanostructured Al–Fe alloys produced by e-beam deposition: static and dynamic tensile properties, Acta Mater. 51 (2003) 4197–4208, https://doi.org/10.1016/S1359-6454(03)00237-4.

[20] H. Ding, Y. Xiao, Z. Bian, Y. Wu, H. Yang, H. Wang, H. Wang, Design, microstructure and thermal stability of a novel heat-resistant Al-Fe-Ni alloy manufactured by selective laser melting, J. Alloys Compd. 885 (2021) 160949, https://doi.org/10.1016/j.jallcom.2021.160949.

[21] C.N. Ekaputra, J.U. Rakhmonov, D. Weiss, J.-E. Mogonye, D.C. Dunand, Microstructure and mechanical properties of cast Al-Ce-Sc-Zr-(Er) alloys strengthened by Al$_{11}$Ce$_3$ micro-platelets and L1$_2$ Al$_3$(Sc,Zr,Er) nano-precipitates, Acta Mater. 240 (2022) 118354, https://doi.org/10.1016/j.actamat.2022.118354.

[22] Z. Bian, C. Yang, H. Zhu, D. Zhao, M. Wang, H. Zhang, Z. Chen, H. Wang, Understanding the creep property of heat-resistant Al alloy by analyzing eutectic phase/matrix interface structures, Mater. Res. Lett. 11 (2023) 205–212, https://doi.org/10.1080/21663831.2022.2136016.

[23] K.E. Knipling, R.A. Karnesky, C.P. Lee, D.C. Dunand, D.N. Seidman, Precipitation evolution in Al–0.1Sc, Al–0.1Zr and Al–0.1Sc–0.1Zr (at.%) alloys during isochronal aging, Acta Mater. 58 (2010) 5184–5195, https://doi.org/10.1016/j.actamat.2010.05.054.

[24] L. Cui, K. Liu, X.-G. Chen, Recent advances in cost-effective aluminum alloys with enhanced mechanical performance for high-temperature applications: a review, Mater. Des. 253 (2025) 113869, https://doi.org/10.1016/j.matdes.2025.113869.

[25] P. Pandey, S.K. Makineni, B. Gault, K. Chattopadhyay, On the origin of a remarkable increase in the strength and stability of an Al rich Al-Ni eutectic alloy by Zr addition, Acta Mater. 170 (2019) 205–217, https://doi.org/10.1016/j.actamat.2019.03.025.

[26] S. Kou, A criterion for cracking during solidification, Acta Mater. 88 (2015) 366–374, https://doi.org/10.1016/j.actamat.2015.01.034.

[27] M.A. Easton, D.H. Stjohn, A model of grain refinement incorporating alloy constitution and potency of heterogeneous nucleant particles, Acta Mater. 49 (2001) 1867–1878, https://doi.org/10.1016/S1359-6454(00)00368-2.

[28] T. Wen, Z. Li, J. Wang, Y. Luo, F. Yang, Z. Liu, D. Qiu, H. Yang, S. Ji, From crack-prone to crack-free: eliminating cracks in additively manufacturing of high-strength Mg$_2$Si-modified Al-Mg-Si alloys, J. Mater. Sci. Technol. 204 (2025) 276–291, https://doi.org/10.1016/j.jmst.2024.04.009.

[29] A. Amon, G.E. Bean, J.-B. Forien, T. Voisin, J.A. Hammons, E.E. Moore, E. Simsek, J. Shittu, K.S. Shanks, K.E. Nygren, Alloy design for additive manufacturing: continuously reinforced Al-Ce nanocomposites, Mater. Des. 250 (2025) 113595, https://doi.org/10.1016/j.matdes.2025.113595.

[30] C. Suwanpreecha, J. Perrin-Toinin, R.A. Michi, P. Pandee, D.C. Dunand, C. Limmaneevichitr, Strengthening mechanisms in Al-Ni-Sc alloys containing Al$_3$Ni

microfibers and Al_3Sc nanoprecipitates, Acta Mater. 164 (2019) 334–346, https://doi.org/10.1016/j.actamat.2018.10.059.

[31] Z. Sun, M. Roscher, M.C. Paolantonio, V. Soh, C. Liu, S.-P. Tsai, C.K. Ng, C.C. Tan, P. Wang, E.A. Jägle, Additive manufacturing of sustainable and heat-resistant Al-Fe-Mo-Si-Zr alloys, J. Alloys Compd. 1010 (2025) 177118, https://doi.org/10.1016/j.jallcom.2024.177118.

[32] R. Ding, J. Deng, X. Liu, Y. Wu, Z. Geng, D. Li, T. Zhang, C. Chen, K. Zhou, Enhanced mechanical properties and thermal stability in additively manufactured Al-Ni alloy by Sc addition, J. Alloys Compd. 934 (2023) 167894, https://doi.org/10.1016/j.jallcom.2022.167894.

[33] M. Klinger, More features, more tools, more CrysTBox, J. Appl. Crystallogr. 50 (2017) 1226–1234, https://doi.org/10.1107/S1600576717006793.

[34] G.K. Williamson, W.H. Hall, X-ray line broadening from filed aluminium and wolfram, Acta Metall. 1 (1953) 22–31, https://doi.org/10.1016/0001-6160(53)90006-6.

[35] J. Shen, W. Zhang, J.G. Lopes, Y. Pei, Z. Zeng, E. Maawad, N. Schell, A.C. Baptista, R.S. Mishra, J.P. Oliveira, Evolution of microstructure and deformation mechanisms in a metastable $Fe_{42}Mn_{28}Co_{10}Cr_{15}Si_5$ high entropy alloy: a combined in-situ synchrotron X-ray diffraction and EBSD analysis, Mater. Des. 238 (2024) 112662, https://doi.org/10.1016/j.matdes.2024.112662.

[36] G.K. Williamson, R.E. Smallman III, Dislocation densities in some annealed and cold-worked metals from measurements on the X-ray debye-scherrer spectrum, Philos. Mag. 1 (1956) 34–46, https://doi.org/10.1080/14786435608238074.

[37] M. Laleh, E. Sadeghi, R.I. Revilla, Q. Chao, N. Haghdadi, A.E. Hughes, W. Xu, I. De Graeve, M. Qian, I. Gibson, M.Y. Tan, Heat treatment for metal additive manufacturing, Prog. Mater Sci. 133 (2023) 101051, https://doi.org/10.1016/j.pmatsci.2022.101051.

[38] J.A. Muñoz, S. Elizalde, A. Komissarov, J.M. Cabrera, Effect of heat treatments on the mechanical and microstructural behavior of a hypoeutectic Al alloy obtained by laser powder bed fusion, Mater. Sci. Eng. A 857 (2022) 144091, https://doi.org/10.1016/j.msea.2022.144091.

[39] G. Luo, H. Chen, Y. Li, C. Yang, L. Hu, S. Ma, H. Wang, Z. Chen, Y. Wu, M. Wang, H. Wang, Improved elevated-temperature strength and thermal stability of additive manufactured Al–Ni–Sc–Zr alloys reinforced by cellular structures, Addit. Manuf. 90 (2024) 104313, https://doi.org/10.1016/j.addma.2024.104313.

[40] Z. Yang, C. Chen, D. Li, Y. Wu, Z. Geng, V. Konakov, K. Zhou, An additively manufactured heat-resistant Al-Ce-Sc-Zr alloy: microstructure, mechanical properties and thermal stability, Mater. Sci. Eng. A 872 (2023) 144965, https://doi.org/10.1016/j.msea.2023.144965.

[41] S. Thapliyal, S. Shukla, L. Zhou, H. Hyer, P. Agrawal, P. Agrawal, M. Komarasamy, Y. Sohn, R.S. Mishra, Design of heterogeneous structured Al alloys with wide processing window for laser-powder bed fusion additive manufacturing, Addit. Manuf. 42 (2021) 102002, https://doi.org/10.1016/j.addma.2021.102002.

[42] G. Rödler, F.G. Fischer, J. Preußner, V. Friedmann, C. Fischer, A. Weisheit, J. H. Schleifenbaum, Additive manufacturing of high-strength eutectic aluminium-nickel alloys – processing and mechanical properties, J. Mater. Process. Technol. 298 (2021) 117315, https://doi.org/10.1016/j.jmatprotec.2021.117315.

[43] A. Plotkowski, K. Sisco, S. Bahl, A. Shyam, Y. Yang, L. Allard, P. Nandwana, A. M. Rossy, R. Dehoff, Microstructure and properties of a high temperature Al–Ce–Mn alloy produced by additive manufacturing, Acta Mater. 196 (2020) 595–608, https://doi.org/10.1016/j.actamat.2020.07.014.

[44] K. Sisco, A. Plotkowski, Y. Yang, D. Leonard, B. Stump, P. Nandwana, R. Dehoff, S. Babu, Microstructure and properties of additively manufactured Al–Ce–Mg alloys, Sci. Rep. 11 (2021) 6953, https://doi.org/10.1038/s41598-021-86370-4.

[45] H. Hyer, A. Mehta, K. Graydon, N. Kljestan, M. Knezevic, D. Weiss, B. Mcwilliams, K. Cho, Y. Sohn, High strength aluminum-cerium alloy processed by laser powder bed fusion, Addit. Manuf. 52 (2022) 102657, https://doi.org/10.1016/j.addma.2022.102657.

[46] X. Zhang, L. Li, Z. Wen, T. Ban, Z. Li, R. Shi, T. Zhai, Z. Wang, J. Gao, Z. Peng, Post-heat treatment of laser powder bed fusion fabricated Al–La–Mg–Mn alloy: on intermetallic morphology control and strength-ductility balance, Addit. Manuf. 78 (2023) 103863, https://doi.org/10.1016/j.addma.2023.103863.

[47] T. Klein, T. Wojcik, A. Arnoldt, A hypoeutectic Al-Ni-Mg in situ composite processed by wire-arc additive manufacturing: phase evolution and mechanical behavior, Mater. Des. 222 (2022) 111066, https://doi.org/10.1016/j.matdes.2022.111066.

[48] K.-C. Chang, J.-R. Zhao, F.-Y. Hung, Microstructure, mechanical properties, and fatigue fracture characteristics of high-fracture-resistance selective laser melting Al-Ni-Cu alloys, Metals 11 (2021) 87, https://doi.org/10.3390/met11010087.

[49] J. Bi, L. Wu, Z. Liu, H. Wang, S. Li, J. Wang, Z. Yang, N. Lu, X. Chen, M. D. Starostenkov, G. Dong, Microstructure, mechanical properties and multiphase synergistic strengthening mechanisms of a novel laser additive manufactured AlNi6TiZr alloy, J. Mater. Sci. Technol. 178 (2024) 59–69, https://doi.org/10.1016/j.jmst.2023.08.033.

[50] S. Oeser, J. Preußner, G. Rödler, N. Pirch, A. Weisheit, Laser metal deposition of a near-eutectic Al-Ni alloy, Adv. Eng. Mater. 24 (2022) 2200696, https://doi.org/10.1002/adem.202200696.

[51] R.A. Michi, S. Bahl, C.M. Fancher, K. Sisco, L.F. Allard, K. An, D. Yu, R.R. Dehoff, A. Plotkowski, A. Shyam, Load shuffling during creep deformation of an additively manufactured AlCuMnZr alloy, Acta Mater. 244 (2023) 118557, https://doi.org/10.1016/j.actamat.2022.118557.

[52] C. Wang, F. Wang, H. Xu, J. Hu, X. Di, C. Liu, Y. Guo, High temperature mechanical properties of wire-arc directed energy deposited Al-Ce-Mg alloy, J. Alloys Compd. 1010 (2025) 177304, https://doi.org/10.1016/j.jallcom.2024.177304.

[53] R.A. Michi, K. Sisco, S. Bahl, Y. Yang, J.D. Poplawsky, L.F. Allard, R.R. Dehoff, A. Plotkowski, A. Shyam, A creep-resistant additively manufactured Al-Ce-Ni-Mn alloy, Acta Mater. 227 (2022) 117699, https://doi.org/10.1016/j.actamat.2022.117699.

[54] Q. Jia, Y. Zhuo, Y. Yan, C. Lu, Z. Chen, Y. Cheng, C. Wang, Tensile creep mechanisms of Al-Mn-Sc alloy fabricated by additive manufacturing, Addit. Manuf. 79 (2024) 103910, https://doi.org/10.1016/j.addma.2023.103910.

[55] H. Yi, L. Yang, L. Jia, Y. Huang, H. Cao, Porosity in wire-arc directed energy deposition of aluminum alloys: formation mechanisms, influencing factors and inhibition strategies, Addit. Manuf. 84 (2024) 104108, https://doi.org/10.1016/j.addma.2024.104108.

[56] Q. Dai, Y. Deng, H. Jiang, J. Tang, J. Chen, Hot tensile deformation behaviors and a phenomenological AA5083 aluminum alloy fracture damage model, Mater. Sci. Eng. A 766 (2019) 138325, https://doi.org/10.1016/j.msea.2019.138325.

[57] Y.L. Zhao, Z.Q. Yang, Z. Zhang, G.Y. Su, X.L. Ma, Double-peak age strengthening of cold-worked 2024 aluminum alloy, Acta Mater. 61 (2013) 1624–1638, https://doi.org/10.1016/j.actamat.2012.11.039.

[58] J. Ogawa, Y. Natsume, Cellular automaton model for predicting the three-dimensional eutectic structure of binary alloys, Comput. Mater. Sci. 195 (2021) 110497, https://doi.org/10.1016/j.commatsci.2021.110497.

[59] M. Gündüz, J.D. Hunt, The measurement of solid-liquid surface energies in the Al-Cu, Al-Si and Pb-Sn systems, Acta Metall. 33 (1985) 1651–1672, https://doi.org/10.1016/0001-6160(85)90161-0.

[60] N. Maraşli, J.D. Hunt, Solid-liquid surface energies in the Al-$CuAl_2$, Al-$NiAl_3$ and Al-Ti systems, Acta Mater. 44 (1996) 1085–1096, https://doi.org/10.1016/1359-6454(95)00227-8.

[61] C. Dan, Y. Cui, Y. Wu, Z. Chen, H. Liu, G. Ji, Y. Xiao, H. Chen, M. Wang, J. Liu, Achieving ultrahigh fatigue resistance in AlSi10Mg alloy by additive manufacturing, Nat. Mater. 22 (2023) 1182–1188, https://doi.org/10.1038/s41563-023-01651-9.

[62] S. Bahl, A. Plotkowski, K. Sisco, D.N. Leonard, L.F. Allard, R.A. Michi, J. D. Poplawsky, R. Dehoff, A. Shyam, Elevated temperature ductility dip in an additively manufactured Al-Cu-Ce alloy, Acta Mater. 220 (2021) 117285, https://doi.org/10.1016/j.actamat.2021.117285.

[63] R.A. Michi, A. Plotkowski, A. Shyam, R.R. Dehoff, S.S. Babu, Towards high-temperature applications of aluminium alloys enabled by additive manufacturing, Int. Mater. Rev. 67 (2022) 298–345, https://doi.org/10.1080/09506608.2021.1951580.

[64] W. Ostwald, Studien über die Bildung und Umwandlung fester Körper: 1. Abhandlung: Übersättigung und überkaltung, Z. Phys. Chem. 22 (1897) 289–330, https://doi.org/10.1515/zpch-1897-2233.

[65] F. Li, W. Zhang, D. Li, X. Jia, B.J. Kooi, Y. Pei, Precipitation evolution, aging strengthening and thermal stability in Al–Fe-Mg-Zr eutectic alloy via laser powder bed fusion, Virtual Phys. Prototyp. 20 (2025) e2516663, https://doi.org/10.1080/17452759.2025.2516663.

[66] Z. Chen, Y. Zhao, Z. Zhang, Theoretical and experimental study of precipitation and coarsening kinetics of θ' phase in Al-Cu alloy, Vacuum 189 (2021) 110263, https://doi.org/10.1016/j.vacuum.2021.110263.

[67] X.P. Li, X.J. Wang, M. Saunders, A. Suvorova, L.C. Zhang, Y.J. Liu, M.H. Fang, Z. H. Huang, T.B. Sercombe, A selective laser melting and solution heat treatment refined Al-12Si alloy with a controllable ultrafine eutectic microstructure and 25% tensile ductility, Acta Mater. 95 (2015) 74–82, https://doi.org/10.1016/j.actamat.2015.05.017.

[68] K.E. Knipling, D.C. Dunand, D.N. Seidman, Criteria for developing castable, creep-resistant aluminum-based alloys – a review, Int. J. Mater. Res. 97 (2006) 246–265, https://doi.org/10.1515/ijmr-2006-0042.

[69] E.J. Lavernia, J.D. Ayers, T.S. Srivatsan, Rapid solidification processing with specific application to aluminium alloys, Int. Mater. Rev. 37 (1992) 1–44, https://doi.org/10.1179/imr.1992.37.1.1.

[70] D.J. Lloyd, D. Kenny, The structure and properties of some heavily cold worked aluminum alloys, Acta Metall. 28 (1980) 639–649, https://doi.org/10.1016/0001-6160(80)90130-3.

[71] S. Thangaraju, M. Heilmaier, B.S. Murty, S.S. Vadlamani, On the estimation of true Hall–Petch constants and their role on the superposition law exponent in Al alloys, Adv. Eng. Mater. 14 (2012) 892–897, https://doi.org/10.1002/adem.201200114.

[72] C.H. Henager Jr, Reversing inverse Hall-Petch and direct computation of Hall-Petch coefficients, Acta Mater. 265 (2024) 119627, https://doi.org/10.1016/j.actamat.2023.119627.

[73] X. Zeng, X. Tong, G. Wu, L. Zhang, X. Xiong, L. Li, Strength-isotropy synergy in a rolled Al-Cu-Li alloy through integrated design of recrystallization and aging precipitation, Mater. Des. 260 (2025) 114991, https://doi.org/10.1016/j.matdes.2025.114991.

[74] J. Bai, M. Gao, C. Wang, J. Pei, L. Yang, R. Guan, Role of Er element and two-stage heat treatment in a rheo-extruded Al–Sc–Zr alloy: balance strength and electrical conductivity, Mater. Des. 260 (2025) 115096, https://doi.org/10.1016/j.matdes.2025.115096.

[75] N. Hansen, X. Huang, Microstructure and flow stress of polycrystals and single crystals, Acta Mater. 46 (1998) 1827–1836, https://doi.org/10.1016/S1359-6454(97)00365-0.

[76] H.R. Kotadia, G. Gibbons, A. Das, P.D. Howes, A review of laser powder bed fusion additive manufacturing of aluminium alloys: microstructure and properties, Addit. Manuf. 46 (2021) 102155, https://doi.org/10.1016/j.addma.2021.102155.

[77] F. Li, W. Zhang, B.J. Kooi, Y. Pei, Eutectic aluminum alloys fabricated by additive manufacturing: a comprehensive review, J. Mater. Sci. Technol. 250 (2025) 123–164, https://doi.org/10.1016/j.jmst.2025.06.016.

[78] J.-Y. Xu, C. Zhang, L.-X. Liu, R. Guo, M.-J. Sun, L. Liu, Achieving high strength in laser powder-bed fusion processed AlFeCuZr alloy via dual-nanoprecipitations and

grain boundary segregation, J. Mater. Sci. Technol. 137 (2023) 56–66, https://doi.org/10.1016/j.jmst.2022.07.033.

[79] C. Tang, W. Mo, L. Wang, A. Shang, F. Li, Z. Bai, M. Song, B. Luo, Atomic insight into the shearing behavior of precipitates in an Al-Cu-Mg-Ag alloy, Acta Mater. 268 (2024) 119737, https://doi.org/10.1016/j.actamat.2024.119737.

[80] J. Zhang, J. Gao, S. Yang, B. Song, L. Zhang, J. Lu, Y. Shi, Breaking the strength–ductility trade-off in additively manufactured aluminum alloys through grain structure control by duplex nucleation, J. Mater. Sci. Technol. 152 (2023) 201–211, https://doi.org/10.1016/j.jmst.2022.12.030.

[81] T. Zhang, F. Li, Z. Shu, H. Chen, D. Li, C. Chen, K. Zhou, Cobalt-mediated mechanical properties in as-deposited Ti alloys: from solid solution to eutectoid strengthening, Mater. Sci. Eng. A 952 (2025) 149619, https://doi.org/10.1016/j.msea.2025.149619.